Master's thesis

NTNU
Norwegian University of Science and Technology
Faculty of Engineering
Department of Energy and Process Engineering

Simen Lillekjendlie Nybu

Numerical simulations of fluid flow and particle deposition in a cascade impactor

Master's thesis in Energy and Environmental Engineering
Supervisor: Erling Næss
Co-supervisor: Silje Bordvik
June 2022

NTNU
Norwegian University of
Science and Technology

Simen Lillekjendlie Nybu

Numerical simulations of fluid flow and particle deposition in a cascade impactor

Master's thesis in Energy and Environmental Engineering
Supervisor: Erling Næss
Co-supervisor: Silje Bordvik
June 2022

Norwegian University of Science and Technology
Faculty of Engineering
Department of Energy and Process Engineering

NTNU
Kunnskap for en bedre verden

Abstract

The Iceland Deep Drilling Project (IDDP) is a project aiming to improve the economics of geothermal energy through heat extraction from supercritical geothermal fluids [1]. This may lead to a higher order of power output, due to the increased energy potential. This technology is however under development. One of the reasons for this is the gradual deposition of silica particles from the supercritical steam onto the pipe surfaces and process equipment are of such a high rate, which automatically results in fouling [2].

A numerical model for the simulation of fluid flow and particle deposition representing the IDDP cascade experiment is established using the Ansys 2021 R2 software. A geometry illustrating the cascade impactor is created, and the flow is modelled using this particular model. The concluded remarks of Stordal is employed in the numerical model, namely by imposing the Reynolds stress equation model (RSM) for the turbulence mean flow simulation. Subsequently, particles were injected, and the relative motion of particles were tracked through the various forces and mechanisms acting on the particles.

The particle deposition was monitored and illustrated using the in-built Fluent particle deposition monitor rate, namely the accretion rate. It was discovered that the particle deposition was distributed more uniformly over the domain for the smaller particles. When the pressure in the domain decreased, it was observed that the particle deposition were more concentrated to only a few regions. However, this phenomena deviates from the observations made in the IDDP experimental tests, where an increasing uniformly deposition occurred when the pressure decreased.

The particle deposition was attempted quantified, and a severe overestimation was observed using the accretion rate. It should also be noted that in the lack of a more suitable discrete random walk (DRW) model, the default DRW model of Fluent had to be employed. This model have been found to overestimate particle deposition as well [3]. Thus it was concluded that an enhancement of the particle deposition tracking is recommended.

Sammendrag

Iceland Deep Drilling Project (IDDP) er et prosjekt som sikter seg inn på å forbedre prosessen og øke potensialet til geotermisk energi ved hjelp av varmeutvinning av fluider langt nede i jordskorpen. Disse fluidene har betydelig høye trykk og temperaturer og kan kvalifiseres som superkritiske [1]. Dette kan føre til en høyere effekt oppnådd, som følge av det økte energipotensialet. Denne teknologien er for øvrig fortsatt under utvikling. En av hovedgrunnene til at dette er at det har blitt oppdaget en gradvis avsetning av silica partikler på overflater av rør og utstyr [2]. Dette vil dermed føre til begroing.

En numerisk modell for simulering av strømningsfeltet og partikkelavsetningen i den eksperimentelle kaskadetesten gjort i IDDP er designet ved bruk av programvaren Ansys 2021 R2. En samsvarende geometri til kaskadetesten er modellert, i tillegg til at strømningen er simulert for denne modellen. Stordal konkluderte med at Reynolds Stress Equation Modellen (RSM) er ideell for å simulere turbulensen i strømningen, og denne modellen ble derfor implementert i denne masteroppgaven også. Etter at strømningen var satt ble partiklene injisert, og de ulike kreftene og mekanismene som virket på partikkelen ble implementert for å gi et bilde av hvordan partiklene ville bevege seg i strømningen.

Partikkelavsetningen på veggen i geometrien ble observert og illustrert ved å bruke den innebygde målemetoden kalt akkresjonsrate. Det ble observert at partikkelavsetningen ble fordelt mer jevnt over geometrien for de mindre partiklene. Når trykket i domenet avtok, ble det observert at partikkelavsetningen var mer konsentrert til bare noen få regioner. Dette fenomenet avviker imidlertid fra observasjonene gjort i IDDP kaskadetesten, hvor partiklene ble mer jevnt fordelt ettersom trykket sank.

Partikkelavsetningen ble også forsøkt kvantifisert, men dette resulterte i en stor overestimering ved bruk av den nevnte akkresjonsraten. Det bør også bemerkes at i mangel på en mer passende discrete random walk modell (DRW), måtte standard DRW-modellen til Fluent brukes. Denne modellen har vist seg å overestimere partikkelavsetning også [3], noe som også fører til overpredikasjon av partikkelavsetningen. Dermed ble det konkludert med at det anbefales en forbedring av sporingen av partikkelavsetning for å oppnå et riktigere bilde av den aktuelle avsetningen.

Acknowledgment

I would like thank my supervisor, Prof. Erling Næss, for the continuous support throughout this semester, and helping me completing this master thesis. I gratefully acknowledge my co-supervisor, PhD Candidate Silje Bordvik as well, for all the helpful insights and discussions regarding this thesis.

To Stian Ranøyen Bratsberg, thank you for valuable discussions and insights regarding the understanding and evaluation of the CFD fundamentals.

Contents

Abstract . . . . . **iii**
Sammendrag . . . . . **iv**
Acknowledgment . . . . . **v**
Contents . . . . . **vi**
Figures . . . . . **viii**
Tables . . . . . **x**
Acronyms . . . . . **xi**
1 Introduction **1**
1.1 Background and motivation 1
1.2 Objective 3
2 Summary of the project work **4**
2.1 Literature review 4
2.2 Method 5
2.3 Concluding remarks 6
3 Theory - fluid flow **7**
3.1 Turbulence modelling 7
3.2 Near wall treatment 8
3.3 Wall boundary conditions 8
4 Theory - Particle modelling **10**
4.1 Influencing forces on the particle 10
4.1.1 Drag force 10
4.1.2 Lift force 11
4.1.3 Brownian force 11
4.1.4 Other body forces 12
4.2 Silica concentration 12
4.3 Particle deposition 12
4.3.1 Schmidt number 13
4.3.2 Stokes number 13
5 Flow modelling **15**
5.1 Simulation tools 15
5.2 Geometry 15
5.3 Fluid properties 18
5.4 Meshing 19
5.4.1 Skewness 20

5.4.2 Orthogonal quality . . . 20
5.4.3 Wall treatment . . . 23
5.5 Simulation setup and flow considerations . . . 25
5.6 Numerical residuals . . . 26
5.7 Grid convergence . . . 27
6 Particle modelling . . . 29
6.1 Assumptions . . . 29
6.2 Particle implementation . . . 29
6.3 Numerical schemes and time steps . . . 30
6.4 Tracking parameters . . . 31
6.5 Particle injection . . . 32
6.6 Particle Forces and turbulent dispersion implementation . . . 32
6.7 Turbulent dispersion . . . 33
6.8 Particle deposition . . . 33
7 Results and discussion . . . 36
7.1 Flow simulation . . . 36
7.2 Particle simulation . . . 40
7.2.1 Particle trajectories . . . 40
7.2.2 Particle velocities . . . 43
7.2.3 Accretion rate . . . 43
8 Conclusion . . . 49
9 Further work . . . 51
Bibliography . . . 52
A Resulting figures and plots . . . 55
B Code listing . . . 61
C Evaluation of the master thesis . . . 63

Figures

1.1 Illustration of the deposition of silica dust in a silencer line from the IDDP [8] . 2

2.1 Force comparison of a particle-wall interaction with a radius of 50 nm 5

5.1 Illustration of the IDDP cascade impact test 16
5.2 The cascade impactor 16
5.3 Dimensions of the case studied 17
5.4 Representation of the geometry 18
5.5 Representation of the skewness of the mesh 21
5.6 Representation of the orthogonal quality 22
5.7 Representation of the boundary layer 23
5.8 Representation of the back wall line, used to plot the wall shear and y^+ value . 24
5.9 The wall shear along the back wall line 25
5.10 Representation of the residual values 26
5.11 Representation of wall shear in the y direction plotted along the back wall line . 28

6.1 The relative error of the analytic and trapezoidal schemes based on the trapezoidal scheme with restricted time step of $\Delta t = \tau_p/2$ fetched from Stordal [3] 31
6.2 The deposition of silica from superheated steam 35
6.3 The scaling of silica on the different orifices in the experiment 1 of the IDDP cascade test 35

7.1 Illustration of the pressure contour of the fluid flow between the inlet and orifice 2 37
7.2 Illustration of the measuring points 37
7.3 The pressure contours of the fluid flow between the inlet and orifice 2 38
7.4 The velocity vectors of the fluid flow between the inlet and orifice 2 39
7.5 The velocity magnitude at the given measurement points 39
7.6 The streamlines of the fluid flow 40
7.7 The residence time of the 100 nm particles 42
7.8 Illustration of the particle trajectory of the incomplete particle with the longest residence time 42
7.9 The accretion rate on the domain with a particle size of 100 nm 44
7.10 The accretion rate on the domain with a particle size of 10 nm 45
7.11 The accretion rate on the domain with a particle size of 1 nm 45
7.12 The accretion contour representing the particle deposition between orifice 5 and 6 46

7.13 The accretion contour representing the particle deposition between orifice 7 and 8 47

A.1 The pressure contour of the fluid flow after injecting particles 55
A.2 The residence time of the 10 nm particles simulated with the analytical numerical scheme 56
A.3 The particle trajectory of the longest lasting 10 nm particle 56
A.4 The particle trajectory of the longest lasting 10 nm particle 57
A.5 The residence time of the 1 nm particles simulated with the analytical numerical scheme 57
A.6 The velocity magnitude of the 100 nm particle trajectories 58
A.7 The velocity magnitude of the 10 nm particle trajectories 58
A.8 The velocity magnitude of the 1 nm particle trajectories 59
A.9 The pressure contour of section two between orifice 5 and 6 59
A.10 The velocity magnitude of the particles in section two between orifice 5 and 6 . 60
A.11 The velocity magnitude of the particles in section three between orifice 7 and 8 60

Tables

5.1 Scaling on orifices 17
5.2 The properties of the supercritical water at different operating conditions 19
5.3 Skewness values and its respective quality characteristics 20

6.1 Representation of the Stokes number at the different pressure regimes given a particle diameter of 100 nm 30
6.2 Properties of the silica particle 32
6.3 Representation of the Cunningham correction factor at the different orifices and particle diameters 33

7.1 The pressure at the different points in the domain 36
7.2 The Schmidt number at the different sections and particle diameters 41
7.3 The accretion rate when injecting different particle sizes 47
7.4 The accretion rate at the different sections 48
7.5 The scaling at the different sections 48

Acronyms

CFD Computation Fluid Dynamics. 3

DLVO theory of particle interactions named after Derjaguin and Landau, Verwey and Overbeek. 4

DPM Discrete Phase Model. 29

DRW Dicrete Random Walk. iii

IDDP Iceland Deep Drilling Project. iii

ODE Ordinary Differential Equation. 30

PDE Partial Differential Equation. 30

RSM Reynolds Stress Model. iii

Chapter 1

Introduction

1.1 Background and motivation

The present study is part of an ongoing study by the Department of Energy and Process Engineering at NTNU in cooperation with Equinor on the Iceland Deep Drilling Project (IDDP).

The need and growing demand of heating and power production is a well-known issue in the world today as the population grows. There is also an increasing emphasis that the power produced is required to be green, namely not produced from fossil fuels. This is regarded as a sustainable solution to the climate problem in the world. Consequently, there have been developed and investigated numerous energy-efficient and non-polluting energy producing systems. One of these systems are developed using geothermal energy, which is considered a renewable energy resource. The geothermal energy is also considered a relatively affordably source of energy, since it is based on the heat recovered from the ground. However, the geothermal energy has its limitations due to limited resources worldwide and technological insight [4]. One of the leading countries in the world, who derive approximately 60 % of their energy from geothermal energy is Iceland [5]. As a result, the IDDP was constituted to further expand the technological insight on geothermal energy. The primary object of the IDDP was to find supercritical steam at 450-550 °C at drillable depths, and the objective was to use this geothermal fluid as an energy source [1]. Soon, Norway must account for a life without the oil, and as a result it could be beneficial to investigate the possibility of implementing this particular energy utilization in the Norwegian energy sector as well.

This technology is however still at the development stage, where one of the major drawbacks is characterized as the gradual deposition of solid silica particles (SiO_2) from the supercritical steam onto the pipe surfaces and process equipment [2]. This deposition results in fouling of the equipment, and it is also regarded as a familiar problem since silica is the most common chemical compound in the Earth's crust and a major component in most geothermal reservoirs, as noted by Heuvel et al [6]. The fouling phenomena arises when the gravitational and fluid-dynamic forces do not influence the particles. In essence, the particle size must be 1 μm or smaller, since the larger particles will be influenced by these forces and will therefore not adhere to the surface [7]. This results in distortion of the turbine blades and an increase in surface roughness, leading to a lower efficiency.

These fouling issues must be addressed before a utilization of this particular energy re-

Figure 1.1: Illustration of the deposition of silica dust in a silencer line from the IDDP [8]

source can be achieved. Hence, the goal of this thesis is based on the investigation of this fouling phenomena, with regards to the existing experimental studies put through by the IDDP. However, the greatest emphasis is placed on the experimental study on silica in superheated steam of the IDDP-1 exploratory geothermal well in Krafla by Kemía and Landsvirkjun. Extensive test were performed to quantify the precipitated matter, and to obtain an overview of where the major silica scaling occurred through an experimental cascade impact test put through by Kemía and Landsvirkjun [8]. The test investigated is a supercritical flow, with high Reynolds number causing turbulence. Hence, a numerical model for the simulation of particle deposition representing the IDDP-1 cascade experiment is developed by implementing a turbulence model for solving the governing equations of the fluid flow. In addition, the forces influencing the dispersed particles in a turbulent gas flow are implemented. These forces are related to the particle deposition and are similar to the ones introduced in the project work of Stordal [3].

1.2 Objective

The main focus of the project work will be to examine the behaviour of the extracted steam during the depressurization process.

The following tasks will be considered:

- The main findings from the project work on the influence of electrostatic charging on particle deposition/adhesion to solid walls shall be summarized and programmed in a suitable computer language.
- A numerical model for the simulation of particle deposition representing the IDDP-1 experiments shall be developed, and simulations shall be carried out and compared to available experimental results.
- A set of measurements of the NTNU particle precipitation rig shall be carried out, and the results shall be compared to numerical calculations and/or available theoretical results.
- Proposals for further work shall be made

This master's thesis is a continuation of the project work of Nybu [9] and the master's thesis of Stordal [3] and Paulsen [10]. The findings in the project work are summarised in chapter 2.

Based on the background and motivation, the scope of this thesis is limited to submicron particles dispersed in a medium of supercritical steam at 400-550 °C. The results of the experimental tests are also of great significance since they are used for validation purposes of the numerical model. Hence, these results lay the foundation of the specific fluid flow, which is necessary to obtain sufficiently correct particle tracks of the silica particles. The objective of this master thesis is restricted to simulate the particle trajectories of particle in the size range of 1 nm, 10 nm and 100. Then, the particle deposition of these three particle diameters are compared. Afterwards, the influence of a varying pressure is investigated. In this matter, an overview of where the deposition of the particles will occur in the domain would be obtained. In addition, the variation of where the deposition particles in the different pressure regimes would be observed as well.

The simulation of the numerical model for the fluid flow and particle deposition is established using the ANSYS 2021 R2 software. Here the geometry, meshing, simulations and post processing are completed.

Originally, the experimental study was planned as a part of this master study. The result of this was to be compared to the numerical calculations. As this experiment was delayed, more time and effort was spent on the modelling work. With limited previous experience in computational fluid dynamics (CFD) modelling, a steep learning curve was necessary to familiarize with the ANSYS software and to provide and critically evaluate a CFD model for this complex geometry. A deeper evaluation of the master thesis is described in appendix C.

Chapter 2

Summary of the project work

The main focus of Stordal and this master thesis is on the fluid dynamics and fluid flow of the particles. However, the project work of Nybu consisted of an investigation of the interacting forces between submerged particles. The emphasis of the project work was to quantify and describe these forces to determine if adhesion of particles would occur. In the following chapter, the main findings from the project thesis are summarized and it can be received upon request.

2.1 Literature review

An investigation of the principal interacting forces causing fouling, mainly the van der Waal and electrostatic forces, is carried out. The important aspects are the interaction between the particle and the pipe wall resulting in the particle deposition, and the particle-particle interaction, yielding a thicker layer of deposition due to the agglomeration of the particles [7].

Several studies regarding the interacting forces between submerged particles and particles-wall interactions have been performed. One central theory explaining this phenomenon is the theory called DLVO, developed by Derjaguin, Landau, Verwey and Overbeek [11]. The DLVO theory attempts to model the two main forces acting on the particle, the electrostatic repulsive force and the attractive van der Waal force. In principle, this theory describes the stability of a colloidal system, where a colloidal system may consist of solids dispersed in liquids, liquid droplets dispersed in liquids, or solids dispersed in gases [12]. The importance of investigating the stability of the system is directly linked to the adhesion of particles. A system is regarded as unstable if the attractive forces dominate and the particles adhere to one another.

Subsequently, The DLVO theory is determined by the sum of the van der Waal and electrical double layer forces between two surfaces. These forces arise due to the Brownian motion, which is a random and uncontrolled movement of the particles in a fluid as these particles are colliding with the fluid phase particles. This is caused by the thermal motion of the molecular agitation of the liquid medium [13].

Both the adhesive and repulsive force depends on and varies with the operating medium and its properties. The adhesive van der Waal force is a function of the particle size R, the separation distance D and the Hamaker constant A. The latter is a function of the Boltzmann constant, $k = 1.380649 \cdot 10^{-23} J/K$, the thermodynamic temperature, T, and the dielectric constant of the three medias. The dielectric constant for the particle, the wall and the intervening

media is denoted as ϵ_1, ϵ_2 and ϵ_3, respectively. In addition, the main electronic adsorption frequency in the UV, ν_e, typically around $3 * 10^{15} s^{-1}$ has been implemented into the equation. Lastly, the refractive index of the media which describes how fast light travels through the material has been implemented. This is represented by n_1, n_2 and n_3 for the interacting particle, the wall and the intervening media [14]. Israelachvili expressed the Hamaker constant and the resulting van der Waal force as:

$$A = \frac{3}{4} k_B T \left(\frac{\epsilon_1 - \epsilon_3}{\epsilon_1 + \epsilon_3} \right)^2 + \frac{3h\nu_e}{16\sqrt{2}} \frac{(n_1^2 - n_3^2)^2}{(n_1^2 + n_3^2)^{3/2}} \tag{2.1}$$

and

$$F_{vdW}(D) = -\frac{AR_{par}}{6D^2} \tag{2.2}$$

The repulsive electrostatic force was formulated by Rimai and Quesnel as a function of the size of the particle, R, the separation distance D, the surface charge density σ and the dielectric constant of the particle and the operating media, ϵ_0 and ϵ_m respectively [15].

$$F_{el} = \frac{\pi R^4 \sigma^2}{\epsilon_0 \epsilon_m (R + D)^2} \tag{2.3}$$

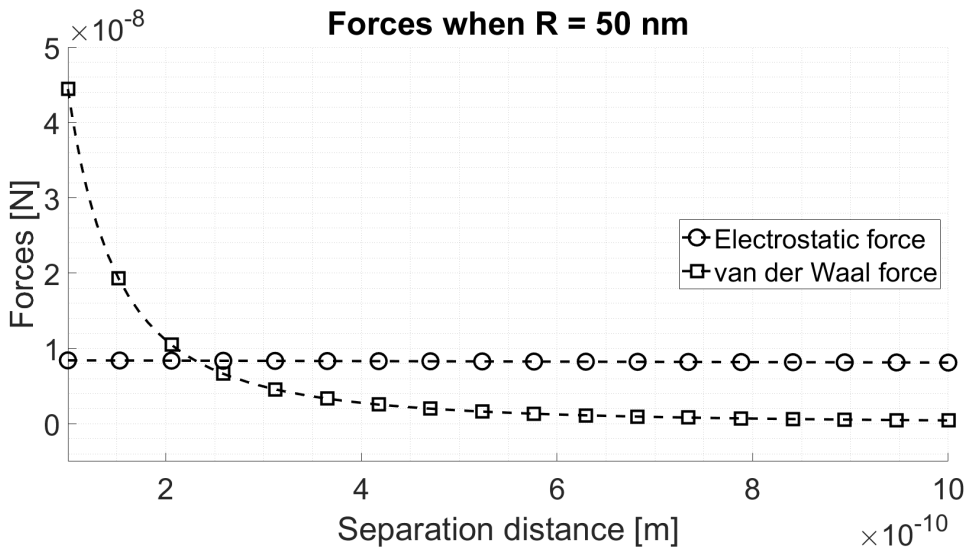

Figure 2.1: Force comparison of a particle-wall interaction with a radius of 50 nm

2.2 Method

Since the working medium is water ranging from 400 to 550 °C and 100 to 400 bar, the properties of the fluid had to be calculated and implemented into equation 2.1 and 2.2. An overview of how the van der Waal force behaves through changes in temperature and pressure could

then be obtained. Afterwards the adhesive and repulsive forces, equation 2.2 and 2.3 respectively, were calculated to quantify and obtain an overview of the magnitude the interacting forces. These numerical calculations were performed and plotted using MATLAB.

2.3 Concluding remarks

The van der Waal force operating in supercritical steam was determined to decrease when the temperature is at its lowest and the pressure at its highest under the operating conditions. The results also yields that the van der Waal interaction between a particle and a surface is in higher order of magnitude than between two particles. When the repulsive electrostatic force is introduced in the particle-surface interaction, it is concluded that the van der Waal force dominates at the smallest separation distances between the two bodies. However, when both the separation distance and the particle radius increase, the importance of the electrostatic force dominates the interaction. Meaning that when the separation distance is small there will be adhesion between the particle and the surface, while a repulsive force is expected when the separation distance and the particle size increase. This can be expressed through figure 2.1

The identical conclusion is not obtained when examining the particle-particle interaction. In this case, the electrostatic force is dominant at all separations. This results in no agglomeration at all in this system, which deviates from the available theory [15].

Chapter 3

Theory - fluid flow

In the following chapter the turbulence model, the near wall treatment and the wall boundary condition is introduced. The governing equations of the fluid flow are those of mass, momentum and energy conservation. The flow is assumed incompressible and steady, which yields the same reading of the governing equation as described in the master thesis of Stordal [3].

3.1 Turbulence modelling

This master thesis is a continuation of Stordal [3], the concluding remarks of the suitable turbulence model has been implemented. Stordal employed the Reynolds stress equation model (RSM) for the turbulence simulation based on the work of Tian and Ahmadi, as this model showed good agreement with experimental, numerical and empirical results with ambient air. The RSM model was also proven to be the most accurate regarding the deposition of particles, since it abandons isotropic eddy-viscosity hypothesis, which is proven to lead to inaccurate predictions of particle deposition [16].

This model is also the most elaborate turbulence model, as the RSM model closes the Reynolds-averaged Navier-Stokes equations. This is done by solving the transport equations for the Reynolds stresses together with an equation for the dissipation rate. It accounts for the effects of streamline curvature, swirl, rotation and rapid changes in strain rate in a more rigorous manner than the two-equation models. To account for all of this, seven transport equations must be solved in 3D, leading to an increase in computational time. For a thorough derivation of these RSM turbulence model equations, the reader is referred to the master thesis of Stordal and the Theory guide of Ansys Fluent [17].

Stordal investigated the particle deposition for a straight channel flow and decided to use the ϵ-based RSM model as it performs better for these kinds of flows. This default RSM model of Fluent was discovered to overestimate the wall-normal mean fluctuating velocity, and a boundary layer model for the wall-normal mean fluctuating velocity was introduced by Stordal.

However, when operating with a 3D flow, some swirling effects will occur as well, and as noted by the Ansys Fluent theory guide the ω-based RSM model is ideal for modelling these flows [17]. The stress-omega model is also excellent for a wide range of turbulent flows. Furthermore, low Reynolds number modifications and surface boundary conditions for rough

surfaces can also be employed using this model by enabling Low-Re Corrections and shear flow corrections. In the stress-omega RSM model, corrections to improve the accuracy in predicting free shear flows can be applied by enabling the shear flow corrections option.

3.2 Near wall treatment

The design of the near wall turbulence modelling is regarded as particularly important for predictions of the particle deposition. The meshing of the geometry in these areas are therefore crucial to a meaningful solution.

There are several guidelines to near wall meshing in the Ansys Fluent theory guide, depending on the turbulence model of choice[17]. In section 5.5, the turbulence model is discussed further, but a key point in the mesh design of most of the turbulence models is to account for the turbulence near the wall by adjusting the dimensionless wall distance, $y+$-value denoted by Gersten as [18]:

$$y^+ = \frac{yu_f}{\nu} \tag{3.1}$$

where y is the absolute distance from the wall, ν is the kinematic velocity and u_f is the friction velocity, denoted by $u_f = \sqrt{\tau_w/\rho}$ where τ_w and ρ are the wall shear and density. One can interpret the y^+ value as a local Reynolds number, so the magnitude of the y^+ value determines the importance of the viscous and turbulent processes. When the y^+ value is in the range of 1, it is inside the so-called viscous sublayer ($y^+ < 4$) where the fluid is dominated by the viscous forces. These viscous forces directly influence the particle deposition [3].

When using the stress-omega RSM model there are no option of applying an enhanced wall treatment to resolve the laminar sublayer. However, by enabling the Low-Re Corrections option in the turbulence modelling, this can be accounted for and implemented. For the cases where the sublayer is adjacent to the wall cells, the size of the first cell at the wall (absolute distance from the wall) should be constructed to achieve an y^+ value of around 1.

3.3 Wall boundary conditions

The RSM model requires boundary conditions for the individual Reynolds stress and for the specific dissipation rate. These quantities are derived from the turbulence intensity and a characteristic length, namely the hydraulic diameter. Consequently, the turbulence intensity of the fluid flow has to be determined. This is defined as the ratio of the root-mean-square of the velocity fluctuations, u' , to the mean flow velocity, u_{avg}. It can be derived through the correlation by Blasius for pipe flows according to the Fluent theory guide [17]:

$$I \equiv \frac{u'}{u_{avg}} = 0.16(Re_{d_h})^{-1/8} \tag{3.2}$$

where the Reynolds number with the hydraulic diameter as the characteristic length is defined as:

$$Re_{d_h} = \frac{\rho_f u_{avg} d_h}{\mu_f} \tag{3.3}$$

Chapter 4

Theory - Particle modelling

4.1 Influencing forces on the particle

A particle dispersed in a medium is affected by numerous forces. After the flow field has been determined through an Euler approach, the particles are employed by the Lagrangian approach. This can be characterized as a one way coupling as it is only the fluid affecting the trajectory of the particle, while the particle does not influence the fluid flow. The trajectory of the particles is then influenced by several forces from the fluid flow, where the general carrier flow effects can be represented by the equation of motion of a turbulent flow field as denoted by the Fluent theory guide [17]:

$$m_p\left(\frac{dv_i}{dt_p}\right) = F_{D,i} + F_{L,i} + F_{B,i} + F_i \tag{4.1}$$

Were, m_p is the particle mass and v_i the particle velocity. The left-hand side of equation 4.1 is the inertia force acting on the particle due to acceleration, whereas the right-hand side represents the steady state drag force, lift force, Brownian force and other body forces respectively. These forces are generally described in the forthcoming sections.

Stordal investigated these forces and constructed user defined functions (UDF's) to include the influence these forces have on the particle trajectories. However, the code created by Stordal is only constructed for serial processing, and the Fluent solver of the newer versions (read Ansys Fluent 2021 R2) have deprecated the serial solver [19]. Furthermore, the improved stochastic tracking is activated for all the particle injections, resulting in a massive increase of computational time when the number of particles are increasing as well.

The forces impacting the particle trajectories do however need to be considered. Therefore, it is assumed that the in-built Fluent implementation of these forces is somewhat representative even though it has been noted by Stordal and others that they have some limitations [3].

4.1.1 Drag force

The drag force is regarded as steady state when there is no acceleration between the carrier fluid and the relative velocity of the particle. The fluent application has eight different drag laws for the particles that can be selected.

The Stokes-Cunningham drag law is applicable for sub-micron particles, but the limitation of the law is that it is restricted to particle Reynolds number up to 0.7 ($Re_p < 0.7$). The definition of the Stokes-Cunningham drag law fetched from the Fluent theory guide can be expressed as:

$$F_D = \frac{18\mu_f}{d_p^2 \rho_p C_c} \tag{4.2}$$

where C_c is the Cunningham correction factor, which is calculated using the following formulation:

$$C_c = 1 + Kn(2.514 + 0.8e^{-(0.55/Kn)}) \tag{4.3}$$

Here, Kn is the Knudsen number representing the rarefied gas effects. This can be understood as where d_p is approaching the same order of magnitude as the mean free path of the gas λ. The mean free path approximation is described in the master thesis of Stordal and included in the equation of the Knudsen number:

$$Kn = \frac{\lambda}{d_p} = \frac{\mu_f}{p}\left(\frac{\pi RT}{2}\right)^2 \frac{1}{d_p} \tag{4.4}$$

where R is the specific gas constant of the fluid, and p and T are the mean pressure and temperature of the fluid flow.

4.1.2 Lift force

The second force contributing to the particle trajectory is the lift force generated by the shear flow. These lift forces act on a particle mainly due to velocity gradients in the fluid flow field. Fluent offers several models representing the lift force, where one these applications is the Saffman's lift force. This form of the lift force is intended for small particle Reynolds numbers and is recommended only for submicron particles. A limitation of the Saffman lift force, is that it is not derived for wall bounding shear flows. However, it is proven to be estimating a sufficiently good representation of the lift force for submicron particles by Tian and Ahmadi [16].

The reader is referred to the Ansys fluent theory guide and the master thesis of Stordal for a derivation of this lift force.

4.1.3 Brownian force

In the core of the fluid flow, the particles are mainly affected by the turbulent dispersion, but when the particles are approaching the wall, the dominant force is the Brownian diffusion. The definition of the Brownian motion is described in the summary of the project work in chapter 2.

It was further noted by Stordal that the magnitude of the Brownian motion increases with an increasing particle size and decreases with the fluid rarefication. It is therefore evident that the Brownian force must be included to account for the submicron particle flow near the walls.

In fluent, the implementation of the Brownian motion can be applied for submicron particles, but it is only valid when the particles obey the Stokes-Cunningham drag law ($Re_p < 0.7$). To activate the Brownian motion in Fluent, the energy equation of the fluid flow must be enabled, and a possible heat flux of the system must be set. In this study it is assumed that the system is adiabatic, meaning zero heat flux.

For a derivation of the Brownian force equations, the reader is referred to the Ansys Fluent theory guide [17] and the master thesis of Stordal [3].

4.1.4 Other body forces

As noted in equation 4.1, there are several other forces also contributing to the particle trajectories, for example wall bonding and phoretic forces. The wall bonding forces are represented by the electrostatic and van der Waal forces as described by the DLVO theory in chapter 2. As noted in the project work of Nybu, the adhesive force dominates at the smallest separation distances resulting in adhesion of particles at the wall [9]. The phoretic forces however are categorized as turbo- and thermophoresis and are carefully described in the master thesis of Stordal.

However, by assuming no heat flux on the geometry, resulting in no temperature gradient, the thermophoresis is neglected. For simplicity, and since there is no in-built method of activating the wall bonding forces in Fluent, these forces are not applied to the simulation neither.

4.2 Silica concentration

The concentration of silica in the fluid flow must be determined before injecting the particles into the domain. Fournier and Potter estimated an equation correlating the concentration of silica in water at temperatures ranging from 25 °C to 900 $degree$C. For the reservoir condition at 350 bar and 500 °C, the equilibrium concentration of silica is estimated to be 244mg/kg [20]. The concentration of silica was demonstrated to be a function of the fluid density and temperature. Furthermore, the investigated superheated and supercritical water is prone to several pressure drops when moving along the process plant. As in this study; through the different sections of the cascade impactor. Consequently, the concentration of silica particles in the fluid flow will change accordingly.

4.3 Particle deposition

There are several different methods of determining the particle deposition on the wall. The calculation of the deposition velocity, V_d^+, as a function of the dimensionless particle relaxation factor, τ_p^+, is one of the most used methods. The particle relaxation factor, τ_p is a time scale representing the adjustment of the particle velocity to a changing fluid velocity. This factor is directly linked to the acceleration time from a standstill situation to reaching the fluid velocity.

The deposition velocity is described in the master thesis of Stordal, where it is further introduced that both the deposition velocity and the dimensionless particle relaxation factor,

are functions of the friction velocity. However, the friction velocity is a function of the wall shear, as noted in section 3.2. Unfortunately, this causes some complications regarding the numerical 3D simulation in Fluent.

The Fluent application however, have an in-built method of calculating the accretion ratio along the wall when applying particles to the flow. The accretion rate can be compared to the scaling and accumulation of particles at the wall [21], making it desirable to measure. According to the Fluent theory guide the steady state accretion rate is defined as:

$$R_{accretion} = \sum_{particle=1}^{N_{particles}} = \frac{\dot{m}_p}{A_{face}} \tag{4.5}$$

The accretion rate is displayed in units of accumulated material/(area-time), that is, mass flux, where $\dot{m}_p$ is the mass flow rate of the particle and A_{face} is the area of the cell face at the wall. When the total mass flow rate of the particle is fixed, the accretion rate will vary with the number of particles injected and the area of the face of the cell at the wall.

4.3.1 Schmidt number

The Schmidt number is a function of the momentum diffusivity and the mass diffusivity, yielding a representation of how relevant the deposition of particles is. It is defined as [3]:

$$Sc = \frac{\nu_f}{D_{par}} \tag{4.6}$$

where ν_f is the kinematic viscosity of the fluid and D_B is the diffusivity of particles represented by the following coefficient:

$$D_{par} = \frac{k_B T C_c}{3\pi\mu_f d_p} \tag{4.7}$$

In the case of a low Schmidt number, the particles have a great diffusivity, are very small and are scarcely influenced by the viscosity. This yields a larger probability of deposition since the particles will cross the laminar sublayer more easily. On the contrary, when the Schmidt number is large, the particles are large, with a small diffusivity and the deposition becomes less relevant.

The Schmidt number is usually in the order of $10^{-}2$ - 10^2, depending on temperature for the flows in air or water. Since the temperature of this present fluid flow is of a large magnitude, this value can be exceeded. It was also noted by Gualtiere et al that since the Schmidt number is a characteristic feature of the turbulent flow, no universal value of the Schmidt number can be established [22].

4.3.2 Stokes number

As described in section 4.3, τ_p is an important entity of describing the influence of particles on the fluid turbulence energy and its dissipation on the particles. This quantity is related to the Stokes number through the following correlation:

$$Stk = \frac{u_{avg}\tau_p}{d_h} \tag{4.8}$$

making the Stokes number a useful measurement of the particle influence. For small Stokes number (Stk « 1), the particles are in near velocity equilibrium with the carrier flow and the flow can safely be regarded as a one-way coupling. For large Stokes number (Stk » 1), the particles are no longer in equilibrium with the carrier fluid, leading to significant momentum transfer from the particle to the fluid [23].

Chapter 5

Flow modelling

The fluid flow and silica scaling is simulated and represented by creating a numerical model of the cascade impact test put through by the IDDP-1 project [8], where the implementation method, geometry, mesh and numerical residuals of this model are presented and discussed in the following chapter.

5.1 Simulation tools

The software program utilized for creating the numerical model is Ansys 2021 R2. The geometry is designed and constructed in Ansys Space Claim, whereas the meshing of the given geometry is meshed in Ansys Meshing Solutions while the simulation is carried out in Ansys Fluent 2021. The writing and evaluation of the results are described and summarized in the Ansys post processor program CFD-post.

5.2 Geometry

The IDDP-1 cascade test was a flow test on a DN25/PN250 flow-line connected directly to the wellhead, consisting of 8 orifices with small openings which were inserted in series as illustrated in figure 5.1. In addition, a control orifice was inserted at the end. The pressure dropped step-wise through the orifices, and the pressure drop will cause saturation of minerals in the steam. Then scaling will form in the orifices where the steam impacts the surface of the next orifice. The pressure and scaling rate was monitored and calculated in each chamber. The cascade impactor is shown in figure 5.2. Henceforth, this geometry is chosen for validation purposes. For simplicity, the geometry of the cascade impactor is divided into 8 different sections representing each orifice yielding the possibility of focusing on only one pipe section bounded by two orifices.

According to the IDDP-1 report the steam was flowed through the 8 orifices in series for 23 minutes, where the inlet pressure was 138 bar and the steam temperature was 450 ° C. During the experiment 49 kg of steam flowed through the orifices, yielding a mass flow rate of 0.0355 kg/s ($\frac{49kg}{23min}\frac{1min}{60s} = 0.0355$ kg/s) [8].

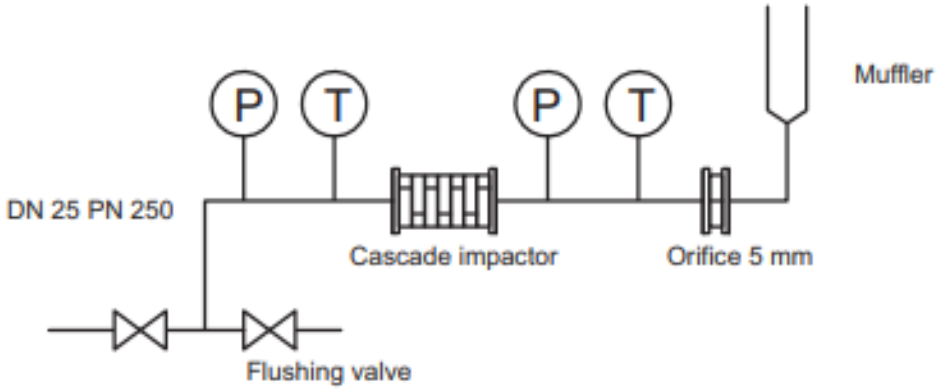

Figure 5.1: Illustration of the IDDP cascade impact test

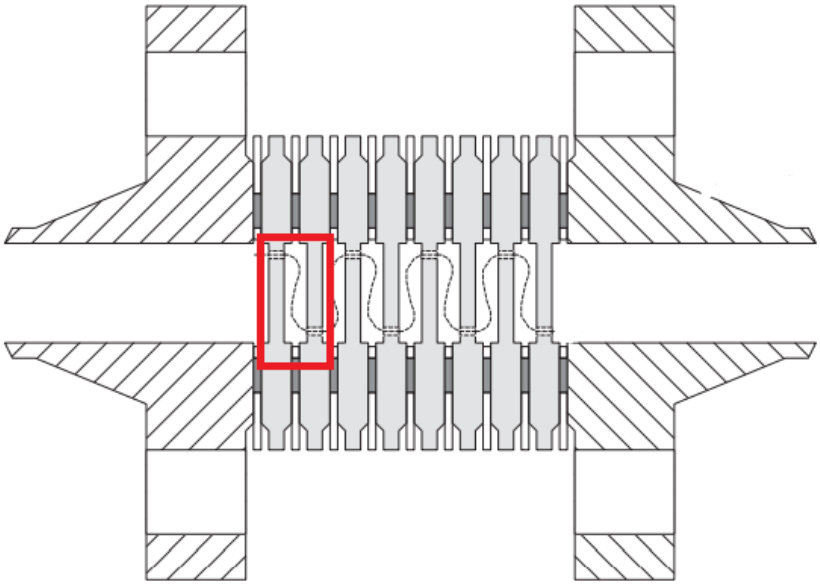

Figure 5.2: The cascade impactor

The results of the experimental cascade test are shown in table 5.1. It is decided that the base case will illustrate the geometry of pipeline between the first and second orifice. As a result, the diameter of orifice 1 and 2 represents the inlet and outlet diameter of the geometry respectively. Hence, that for this base case, the diameter of the inlet and outlet orifice is set to 2.5 mm. The chosen geometry is illustrated with the red square in figure 5.2.

The dimensions of the DN25/PN250 pipeline are fetched from wermac.org giving a pipe

Table 5.1: Scaling on orifices

	Size [mm]	P [bar]	Scale [mg]	Scale/steam [mg/kg]
Orifice 1	2.5	132	4	0.1
Orifice 2	2.5	111	8	0.2
Orifice 3	3.0	93	4	0.1
Orifice 4	3.5	82	3	0.1
Orifice 5	3.0	69	123	2.5
Orifice 6	3.5	53	301	6.1
Orifice 7	4.0	42	286	5.8
Orifice 8	4.0	30	122	2.5
Control orifice 9	5.0	12	10	0.2

diameter of 26.5 mm [24]. The dimensions remaining to be determined are the "thickness" of the orifices, meaning the length of the pipe section in the x direction in figure 5.2, and the length of the inlet and outlet in the x direction. Since there is no available information about the thickness of the orifices in the IDDP-report an assumption of the inlet and outlet length must be determined. It is assumed that the sketch presented in figure 5.2 is correct regarding the dimensions, resulting in a dimension ratio between the sketch and the real pipeline. Consequently, the sketch is imported into SpaceClaim, and the sketch is then adjusted to fit the diameter of the pipe to 26.5 mm. The thickness of the section is then measured to 7.5 mm and the inlet and outlet to 5 mm respectively. This methodology is illustrated in figure 5.3

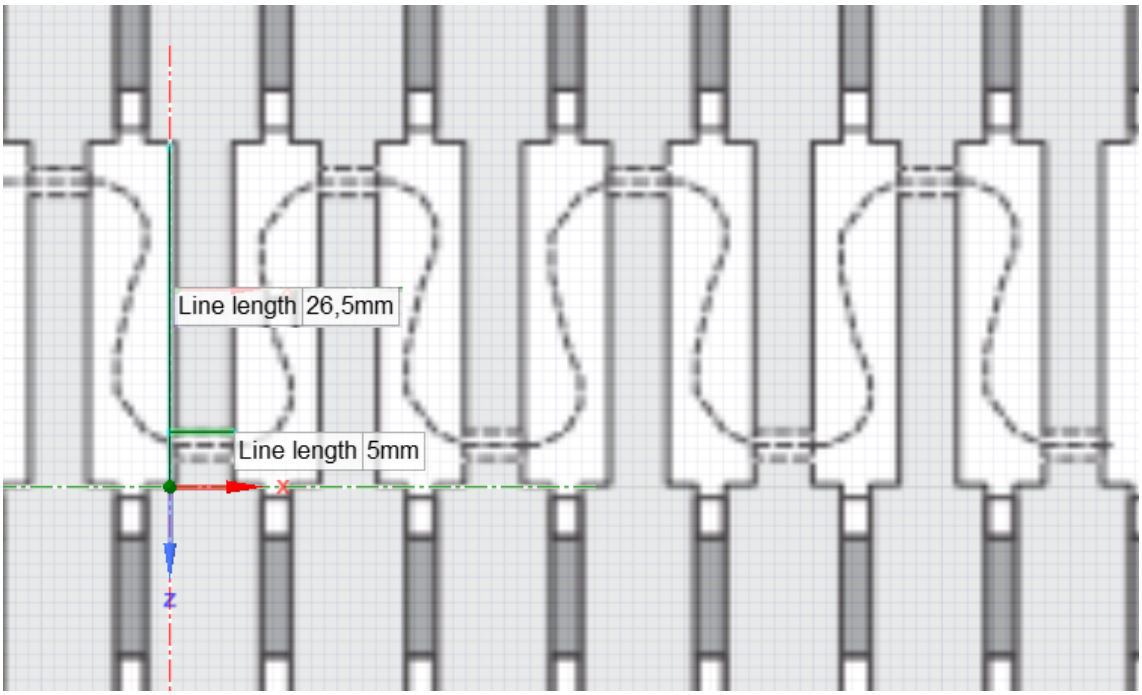

Figure 5.3: Dimensions of the case studied

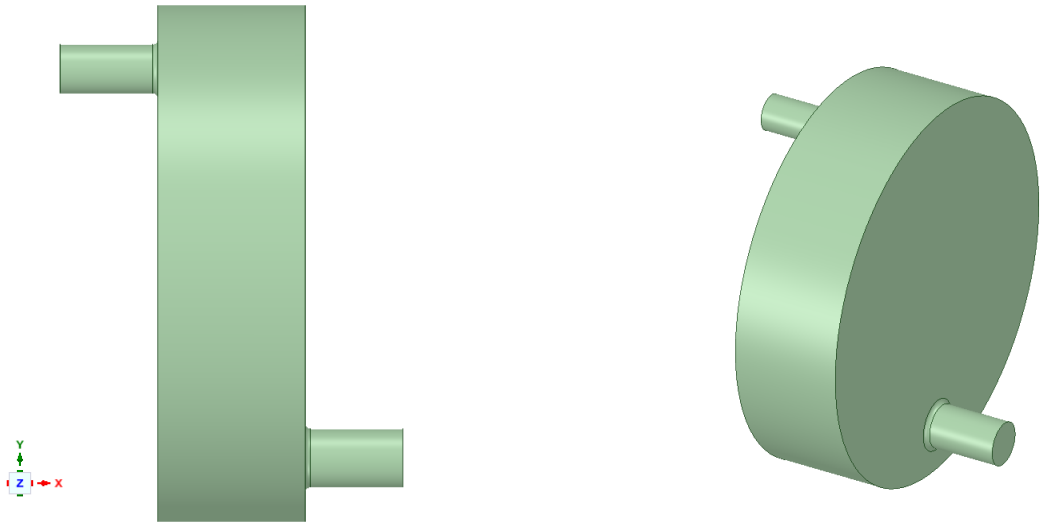

Figure 5.4: Representation of the geometry

All of the needed dimensions are therefore obtained, and a 3D model of the geometry can be designed. It is decided that the geometry must be in three dimensions to account for the complex flow which will in the experimental setup as well. Similarity with the cascade impactor pipeline will also be obtained for this instance. The swirling flow, the turbulence and the diffusion of particles can then be included in the simulation for all the dimensions. However, to account for the sudden change in profile distribution due to the sharp edges at the inlet and outlet, these edges are rounded to prevent and minimize possible flow problems which can arise. The resulting geometry is shown in figure 5.4.

5.3 Fluid properties

By focusing the base case on the pipe section between the first and second orifice, the properties of the water vapour must be set accordingly. The results of the experimental cascade test are used to determine the operating pressure range of the numerical model as represented in table 5.1. Hence, the outlet pressure is set to the pressure at the outlet orifice, namely orifice 2. To prevent case-sensitive results, the properties of the fluid flow is decided to be constant. It is then assumed that the flow is adiabatic and isenthalpic. Hence, the Excel Add-in of the IAPWS-IF97 Water and Steam Properties is implemented to determine the density, viscosity, specific heat and thermal conductivity at the different pressure values fetched from the experimental results in table 5.1. The isenthalpic value is found by inserting the known inlet pressure and temperature at 138 bar and 723 K according to the cascade test [8]. Then, the temperatures at the different pressure stages are adjusted and set to match the isenthalpic value. Afterwards, the fluid properties are calculated based on the steady state temperature and pressure, and the results are shown in table 5.2.

	P [bar]	T [K]	ρ_f $[kg/m^3]$	μ_f [kg/(ms)]	c_p [J/kgK]	k_{th} [W/mK]
Inlet	138	723	48,8999	$2{,}7003e^{-5}$	3128,5652	0,0769
Orifice 2	111	707,2764	39,2415	$2{,}6094e^{-5}$	2949,1813	0,0715
Orifice 3	93	695,9907	32,8148	$2{,}5489e^{-5}$	2820,1545	0,0679
Orifice 4	82	688,7379	28,8951	$2{,}5120e^{-5}$	2737,3832	0,0658
Orifice 5	69	679,7839	24,2724	$2{,}4683e^{-5}$	2635,5979	0,0632
Orifice 6	53	668,1392	18,6003	$2{,}4147e^{-5}$	2504,3448	0,0510
Orifice 7	42	659,6940	14,71381	$2{,}3779e^{-5}$	2410,3475	0,0578
Orifice 8	30	650,0334	10,4796	$2{,}3399e^{-5}$	2303,9680	0,0554
Control orifice 9	12	634,5820	4,1805	$2{,}2786e^{-5}$	2141,1507	0,0515

Table 5.2: The properties of the supercritical water at different operating conditions

It is however noted that under the results of the IDDP experiments, the temperature at the end of the cascade was measured to 292 °C (565 K). This means that the temperature calculated using the isenthalpic assumption deviates with 69 K from the actual temperature at the last orifice. This is probably due to the fact that there are some losses due to heat and pressure loss. Nevertheless, the assumption of isenthalpic behaviour is applied to simplify the simulation.

The necessary properties are then obtained. In addition, it must be verified that the flow investigated is of a turbulent matter. The Reynolds number (equation 3.3) at the inlet must be calculated using the hydraulic diameter of $d_h = 0.0025$ m as the representing length scale. Further, u_{avg} is calculated from the mass flow rate from the cascade test, the density of the fluid (from table 5.2) and the area of the inlet, resulting in $u_{avg} = 148$. Inserting this value into equation 3.3 yields a Reynolds number of 669505.704, and the flow is verified as a turbulent flow.

5.4 Meshing

The resulting operating geometry is of a somewhat complex 3D shape and the fluid flow is of a turbulent matter. This yields a higher importance of the meshing of the geometry to account for all the flow characteristics. Therefore, the meshing of the geometry is regarded as crucial to obtain an adequate numerical solution, as well as reaching a convergence, as the convergence is directly linked to the grid refinement. The quality of the mesh plays a significant role in the accuracy and stability of the numerical computation. The orthogonal quality and the skewness are two frequently used quality measurements, and these are carefully presented in subsection 5.4.2 and 5.4.1.

The geometry is meshed with a patch conforming tetrahedral method with 5 different element sizes of the cells. This method is chosen as it supports 3D inflation, suitable for resolving the boundary layer. Additionally, it has a built-in growth and smoothness control, meaning that the mesher tries to create a smooth size variation based on the specified growth factor [25]. This growth factor is set to the default value, of 1.2. The tetrahedral method is also known as method that can be applied to any 3D volume, regardless of shape or topology, making it desirable to apply to a complex 3D geometry.

A convergence check of the different cell sizes is then performed to determine if the near wall cells are sufficiently small. The convergence check is presented and discussed in section 5.7

5.4.1 Skewness

The skewness is often regarded as the default measurement value of mesh quality, making it crucial to measure before moving on to the simulation. The skewness of the cell represents the difference between the shape of the cell and of an equilateral cell of equivalent volume. According to the definition of the skewness, a value of 0 indicates an equilateral cell and a value of 1 indicates a completely degenerate cell. It is desirable to design a mesh with a low skewness, as highly skewed cells can decrease accuracy and destabilize the solution [25]. The following table is fetched from the Ansys Meshing theory guide, describing the range of skewness values and the corresponding cell quality 5.3.

Value of Skewness	Cell Quality
1	degenerate
0.9 - <1	bad
0.75 - 0.9	poor
0.5 - 0.75	fair
0.25 - 0.5	good
>0 - 0.25	excellent
0	equilateral

Table 5.3: Skewness values and its respective quality characteristics

According to the Ansys Meshing theory guide, a general rule of thumb for a tetrahedral mesh is that the maximum skewness should be kept below 0.95 and the average value less than 0.33. As for 3D, most cells should be good or better, but a small percentage will generally be in the fair range and there are usually even a few poor cells [25]. The maximum average and minimum skewness of the final mesh is represented in figure 5.5, yielding a satisfactory good mesh.

5.4.2 Orthogonal quality

The orthogonal quality is an important measure of quality as well, as convergence difficulties can be encountered when the orthogonality is not accounted for. It is also directly linked to the skewness for tetrahedral cells, as the orthogonal quality is defined as the minimum of the orthogonality and (1 - cell skewness) [25]. The orthogonality is defined to how close the angels between adjacent element faces or edges are to some optimal angle, depending on the relevant topology.

Similarly to the skewness, the orthogonal quality measure ranges from 0 to 1, where 0 is the worst and the cell is regarded as squished and deviates from the optimal orthogonal quality [26]. It is therefore evident that the orthogonal quality must be satisfactory high to lower the possibility of divergence in the simulations. A general rule of thumb is to keep the minimum

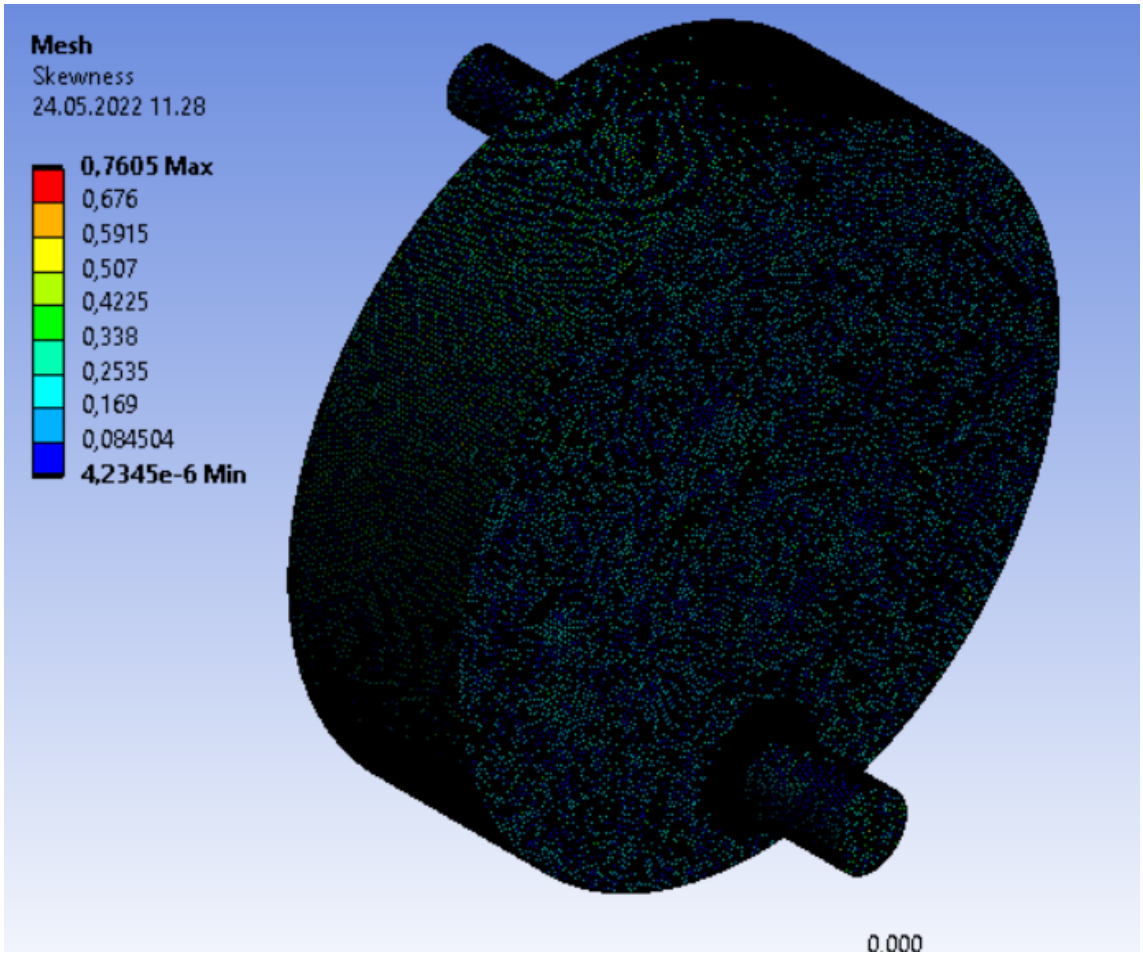

(a) The mesh and skewness values

Mesh Metric	Skewness
Min	4,2345e-006
Max	0,7605
Average	0,1928
Standard Deviation	0,10132

(b) Skewness values

Figure 5.5: Representation of the skewness of the mesh

value above 0.1 to prevent convergence difficulties [27]. The orthogonal quality is measured and represented in figure 5.4.2, well inside the recommendations of the quality values.

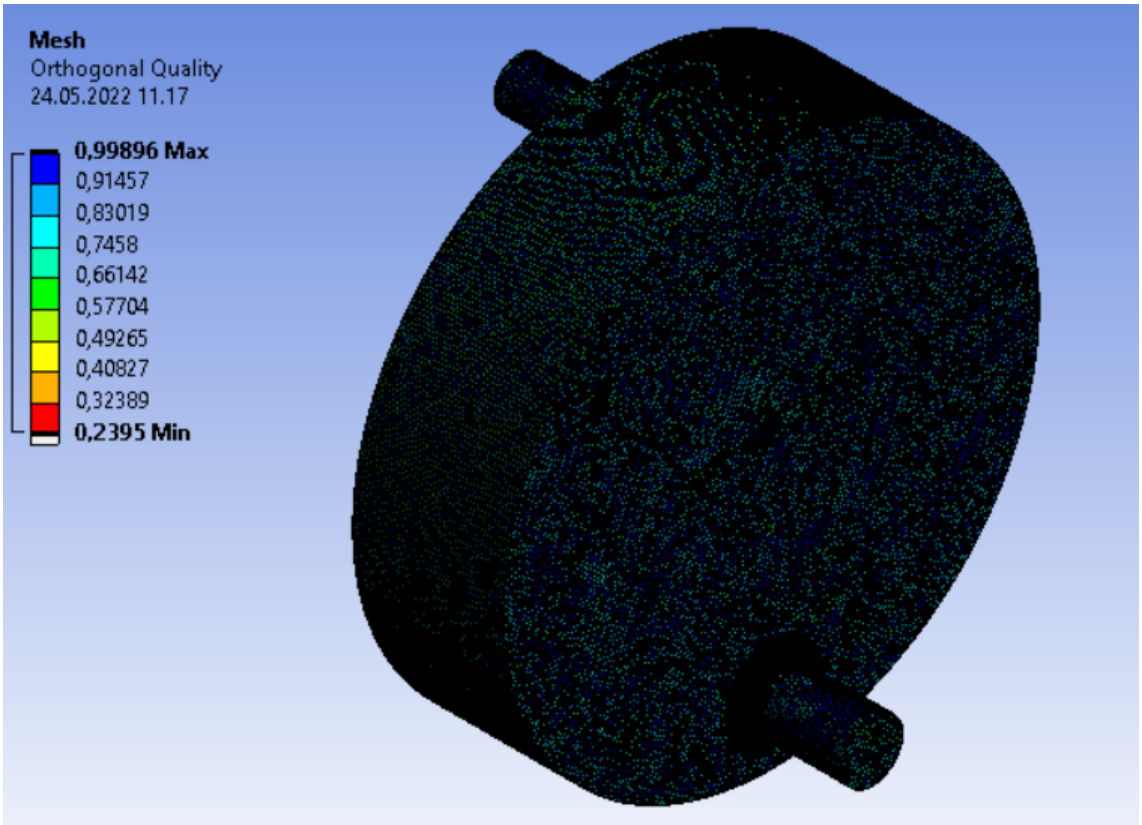

(a) Orthogonal quality of the mesh

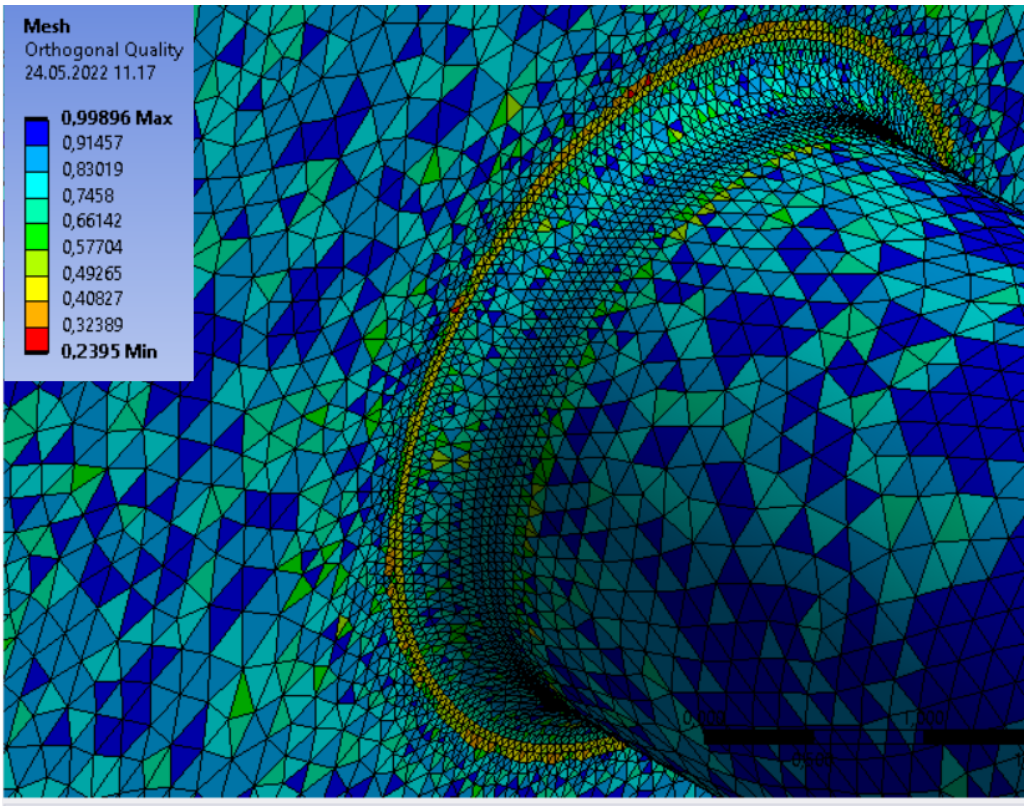

(b) Closer snippet of the mesh at outlet

Figure 5.6: Representation of the orthogonal quality

5.4.3 Wall treatment

As requirements of the mesh have been met and a satisfactory good mesh have been obtained, one of the most central and interesting aspects regarding this master thesis have to be investigated, namely the particle interaction with the walls. A major concern and important emphasis is then put on the resolution of the mesh close to the walls. A poor resolution at the critical regions can dramatically alter both the flow and the particle characteristics. Additionally, the turbulence quantities near the wall have to be resolved since the turbulence plays a dominant role in the transport of mean momentum and other parameters. Consequently, the resolution of the boundary layer (the mesh spacing near walls) plays a significant role in the accuracy of the computed wall shear stress as well.

This particular flow is greatly affected by turbulence, and therefore the significance of solving the near wall treatment increases. In addition, due to the strong interaction between the mean flow and the turbulence, the numerical results for turbulent flows are regarded as more susceptible to mesh dependency than those for laminar flows [17]. At the in- and outlet and at the walls it is therefore necessary to design sufficiently fine meshes to account for the rapid changes and large strain rates.

To resolve the y^+ value and the boundary layer at the wall, a built-in meshing method of inflation in Fluent Meshing was set at the adjacent faces of the wall. It was applied with a total number of 15 layers, with a growth rate of 1.2 and a maximum thickness of 0.025 mm. This is illustrated in figure 5.7. It is usually considered good practice to include between 10 and 15 inflation layers to accurately resolve the boundary layer [28], while the default value of a growth rate of 1.2 of the cells is applied. The resulting maximum thickness had to be decided through trial and error as explained below.

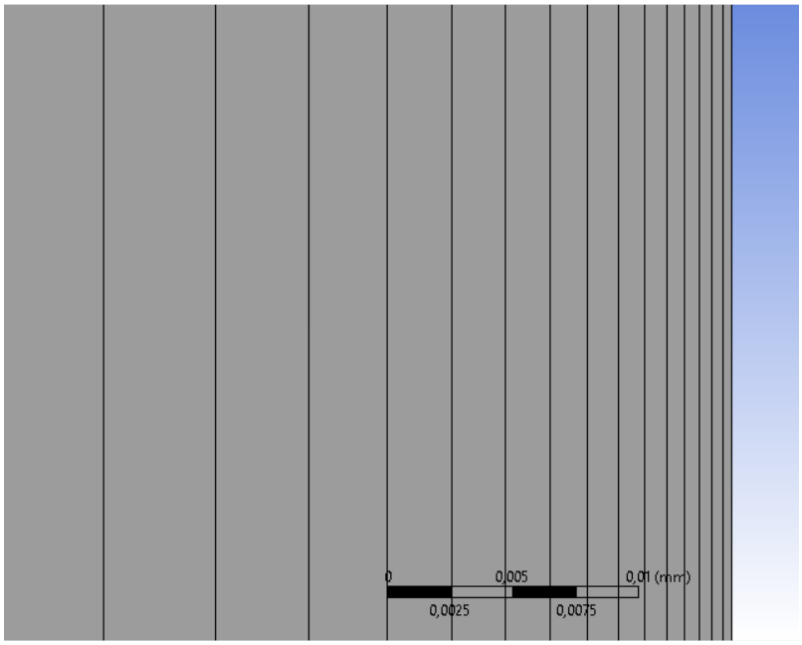

Figure 5.7: Representation of the boundary layer

Since the y^+ value varies with the friction velocity, which again varies with the wall shear, the entire simulation had to be completed to quantify the wall shear and the resulting y^+ value. This resulted in a somewhat iterative process, where the final maximum thickness of the cells had to be determined after a reasonable $y+$ value had been reached. The simulation process is carefully explained in section 5.5.

It is assumed that the largest value of the wall shear will occur at the opposite wall of the inlet, due to the fact that the flow will have a large velocity from the inlet hitting the back wall. This yields that wall shear had to be plotted along the back wall, represented by the yellow line in figure 5.8. This calculation was completed in the CFD post processor. As a result, the maximum thickness of the largest boundary layer cell size was determined to 0.0025 mm, yielding the y^+ values along the back wall illustrated in figure 5.9a. It is evident that the y-plus value varies with the magnitude of the wall shear, represented by the tops on the curve. However, the operating y^+ value is inside the laminar sublayer ($y^+ < 4$), so the boundary layer is considered covered.

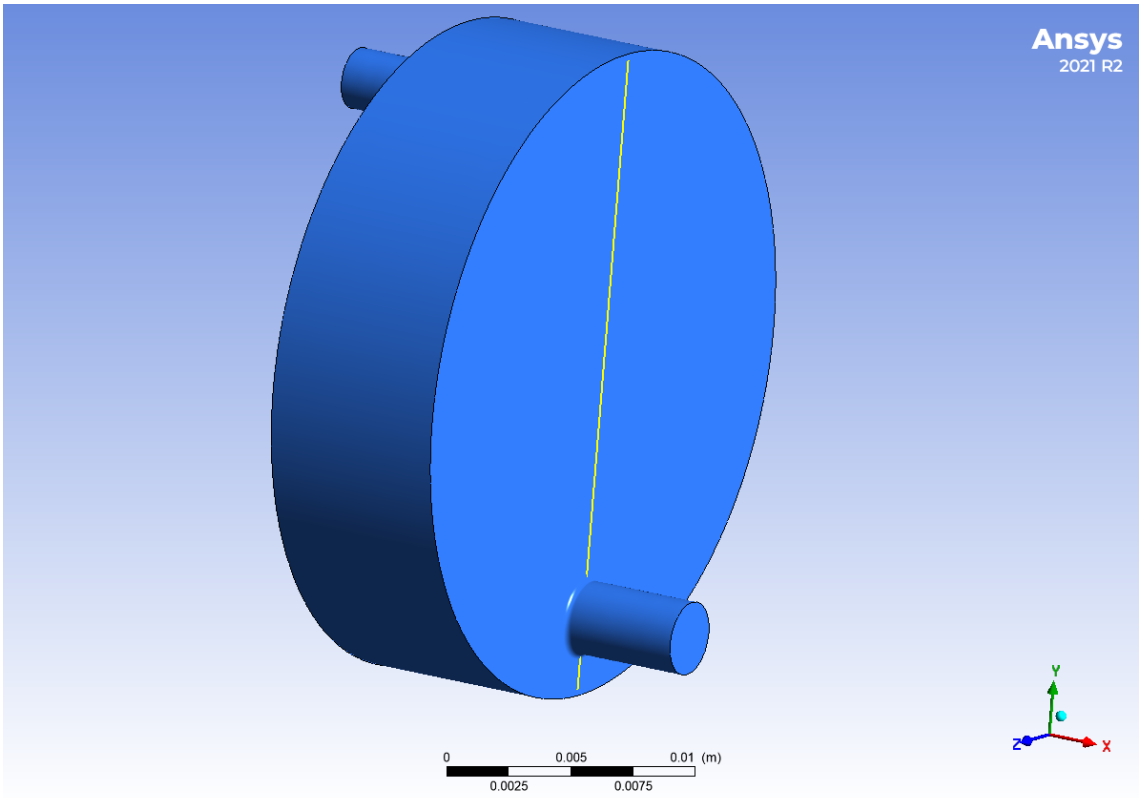

Figure 5.8: Representation of the back wall line, used to plot the wall shear and y^+ value

Confusion can rise, when evaluating the y^+ value at the back wall as demonstrated here. The y^+ value measured will represent the x^+ value since it will be the dimensionless wall distance in the x-direction. The y-value on the x-axis will still be the y-value, representing the y value of the back wall line in figure 5.8. The CFD-post processor interprets the value as the x^+ value however, but denotes it as y^+, resulting in the denotation in figure 5.9a.

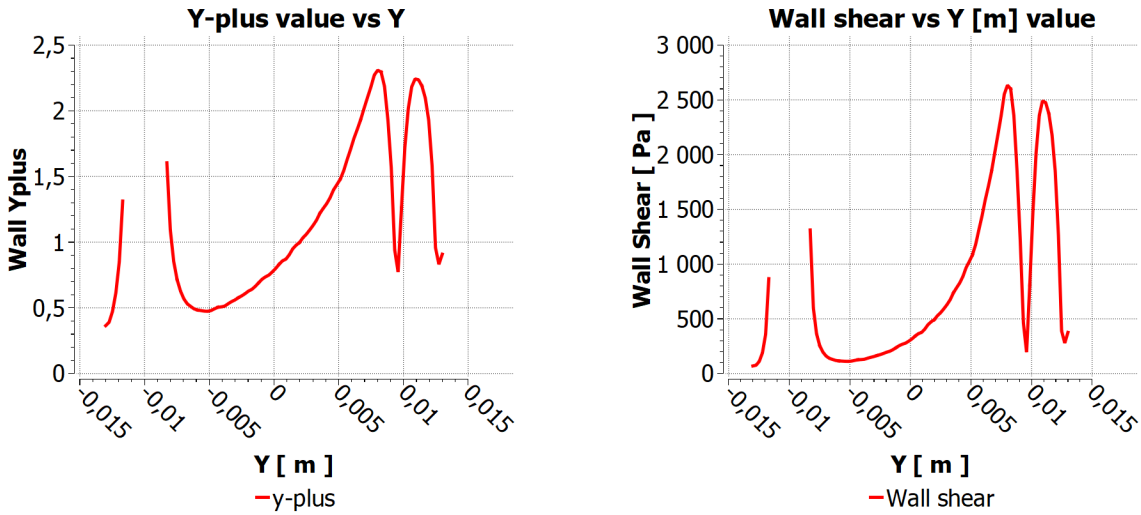

(a) The y^+ value along the back wall line

(b) Closer snippet of the mesh at outlet

Figure 5.9: The wall shear along the back wall line

5.5 Simulation setup and flow considerations

The simulation approach of computing the following incompressible, pressure-driven, turbulent flow has been carefully determined. The pressure-based steady-state solver is employed, as the flow is incompressible and with a constant density.

Regarding the computational model, the RSM omega-stress model is applied, described in section 3. As aforementioned in chapter 1, the object of this master thesis is to compare the results of the different pressure ranges. Consequently, different simulations are implemented to account for the varying pressure. In order, to validate the numerical simulation, the diameter of the outlet and inlet must match the diameter of the orifices. Therefore, in addition to the base case, two other sections of the pipeline are evaluated. These two additional sections are the section between 5 and 6 and the section between 7 and 8. Subsequently, the pressure at the inlet of the geometry is known, and the fluid properties of the supercritical water are updated accordingly to the ones presented in table 5.2.

Before initializing and choosing the solution methods, the boundary conditions of the flow must be determined as well. The inlet is regarded as a mass flow inlet, and the calculated mass flow of 0.0355 kg/s from section 5.2 is applied. The outlet is imposed as a pressure-outlet, setting the outlet pressure equal to the outlet pressure out of orifice 2, 6 and 7. The wall is set as stationary, and a heat rate of 0 W/m^2 is imposed. The no-slip condition is applied as well. Lastly the turbulence intensity I 3.2 is calculated to 2.99 for the base case, and together with the hydraulic diameter of 0.0025 m, these are set as inlet and outlet conditions to initiate the boundary conditions for the Reynolds stresses. The turbulence intensity and hydraulic diameter must be calculated and changes accordingly when evaluating the two other sections.

For the pressure-velocity coupling, the coupled pseudo-transient solution algorithm is employed. In general, segregated methods are faster per iteration, while the coupled algorithm usually requires fewer iterations to converge. The pressure-based pseudo-transient coupled al-

gorithm also obtains a more robust and efficient single phase implementation for steady-state flows. For this reason, the coupled solver is recommended for steady-state simulations, and the one applied in this simulation.

The least-squared cell-based method is used on gradients for constructing gradients at the cell faces, whereas for the spatial discretisation, the second order-scheme is applied for the pressure. A second-order upwind scheme is used on the remaining variables.

The default values of the under-relaxation factors had to be adjusted as well, since unstable and divergent behaviour were observed during the simulations. The under-relaxation factors for pressure and the specific dissipation rate were adjusted from 0.5 and 0.75 to 0.2 and 0.5 respectively.

Before running the calculation, the pseudo transient settings have to be determined as well. The automatic time step method is chosen where the pseudo time step size is calculated internally and used for each equation listed in chapter 24.6.1 in the Ansys Fluent theory guide [17]. The convergence process is also tried controlled by adjusting the Time Scale Factor which simply scales the calculated time step size by a specified value. This Time Scale Factor is adjusted from 1 to 3 to increase the convergence rate.

5.6 Numerical residuals

The numerical residuals represent the errors from solving the governing equations. To achieve a converged solution these values have to be checked and verified. A convergence criterion of 10-3 is set as the limit of the residual value resulting in convergence, and the continuity and the momentum are checked against this limit. The continuity reached a residual value of about 2e-4, whereas the x-,y- and z-velocity only reached a residual value around 1.5e-3. However, as represented in figure 5.10, the solution is in steady state, and the residual values will not deviate much longer.

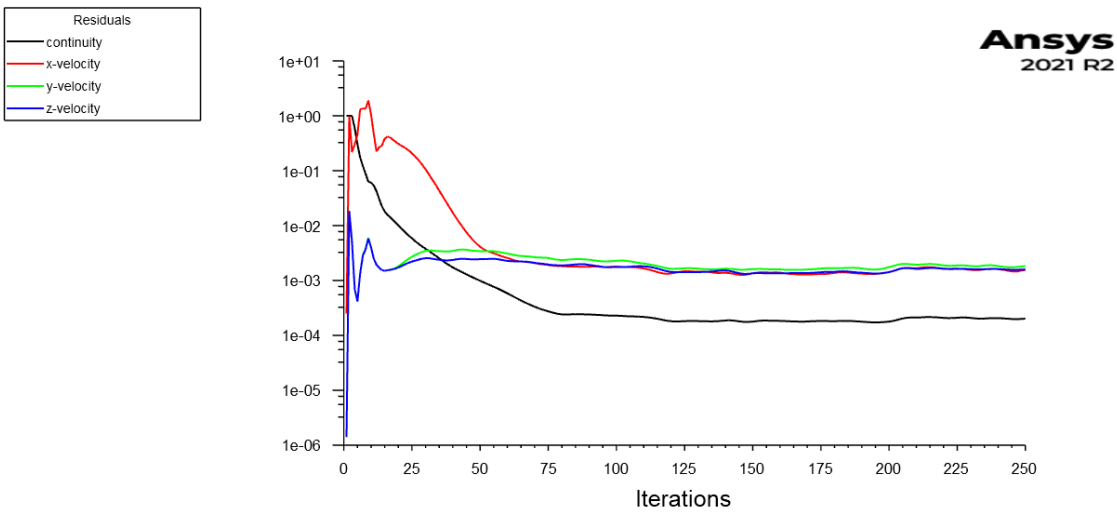

Figure 5.10: Representation of the residual values

As a confirmation of convergence the mass imbalance can be checked through equation 5.1. Due to mass conservation this should be equal to zero, whereas it was calculated below 10^{-5} in the present simulations, and the solution can be regarded as converged.

$$\frac{\sum \dot{m}_{in} - \sum \dot{m}_{out}}{\sum \dot{m}_{in}} \tag{5.1}$$

5.7 Grid convergence

The grid convergence test is done to verify how much the solution is affected by the grid resolution. Before choosing the operating grid resolution a convergence check is done to ensure that the cells are sufficiently small to obtain an adequate solution.

Different meshes have been constructed with different cell sizes. To evaluate the convergence, it is decided to measure the dynamic pressure and the wall shear at two different points at the back wall. The wall shear is evaluated as it is crucially related to the energy dissipation. The dynamic pressure is the kinetic energy per unit volume of the moving fluid in the domain and is often called the velocity pressure. Since the dynamic pressure is directly linked to the velocity, it is also proportional to the calculation of the lift and drag coefficient [29]. The lift and drag greatly affects the particles that are injected into the flow, making the dynamic pressure desirable to use as a convergence check .

The two points evaluated are located at the opposite side of the inlet (inn-wall), and at the center of the back wall, calling it the mid-wall. These two points are illustrated in figure 7.2. They are denoted as mid and inn, displayed with the mid-wall value first. The values of the convergence check is listed in table 5.7

Mesh	Num. of cells	Dyn press: mid/inn	Wall shear: mid/inn
Coarse 1 (0.4 mm)	604100	674.882/534.364	862.204/687.905
Coarse 2 (0.3 mm)	1015335	334.83/3117.4	620.555/1814.05
Medium (0.2 mm)	2657815	335.269/4283.45	621.981/2184.98
Fine 1 (0.15 mm)	4109266	454.088/4760.63	726.989/2318.75
Fine 2 (0.12 mm)	6957749	341.374/4399.98	609.475/2237.11

Here, it is observed that no sufficient convergence value is obtained from the values in table 5.7. The dynamic pressure and wall shear at the mid-wall are quite similar for the coarse 2 and medium mesh, but the values deviate at the other instances. Therefore, it was determined to plot the wall shear in the y-direction of the back wall line 5.8, to obtain an overview of the asymptote of the y wall shear. This is illustrated in figure 5.11.

By investigating these plots, it can be seen that the asymptotic variation is quite similar for the different cell sizes. The variation between the 0.2 mm cell size and the 0.15 mm cell size at the middle of the wall at y=0 deviate with around 100 Pa, which is approximately 25 %. At the extreme point located at approximately y=0.0075 m there is no large deviation between the 0.2 cell size function and the function of the 0.15 cell size.

It is decided that the cell size of 0.2 mm is the one used for the future calculations, since the representing curve is sufficiently close to the ideal asymptote. It would be desirable to

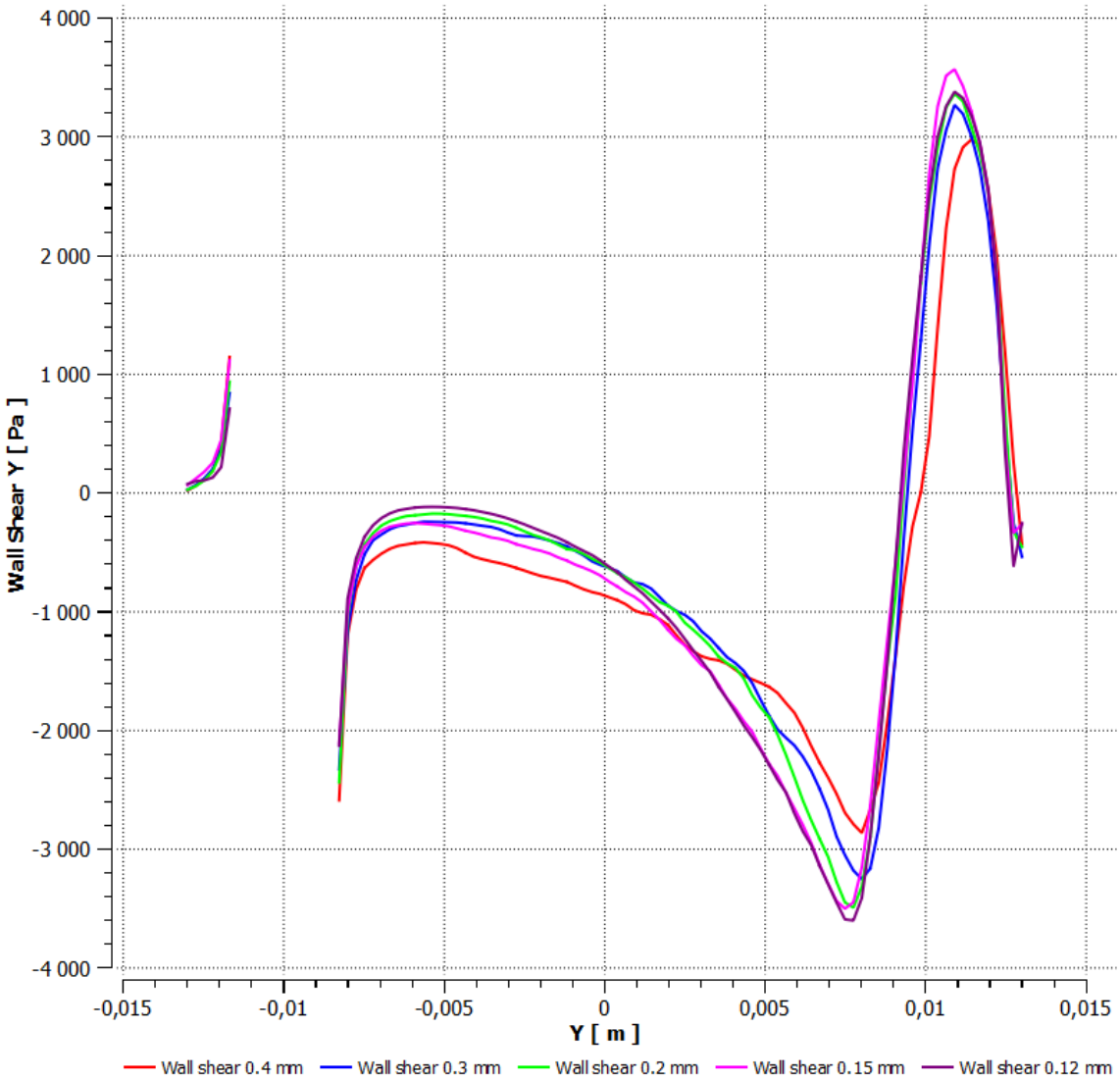

Figure 5.11: Representation of wall shear in the y direction plotted along the back wall line

decrease the cell size even further from 0.12 mm, to observe if an adequate convergence value would be obtained. It is however limited by the fluent software which cannot handle a number of cells of more than 10 million. Another limitation is the increase in computational time when the number of cells increases to this magnitude.

Chapter 6

Particle modelling

In the following chapter, the assumptions regarding the particle injection and the resulting implementation method is described.

6.1 Assumptions

To reduce the uncertainties in the simulations of the particle dispersion and deposition, some assumptions have been made to simplify the calculations. The particles are modelled as non-rotating spheres and injected from the inlet surface, with a uniform diameter distribution of the particles. Particle agglomeration is not examined and the contribution due to particle-particle interaction is neglected. The gravity term is neglected as well, and the temperature gradient is regarded constant resulting in no thermophoresis. To simplify even further, the walls are assumed to be smooth, that is the wall roughness is set to 0. By applying a wall roughness, particle deposition would be enhanced as described by Melo et al [7].

In addition, it is assumed that the mean velocity of the injected particles is of a relatively small magnitude resulting in a lower particle Reynolds number ($Re_p < 0.7$). With this assumption employed, the Stokes-Cunningham drag is applicable. It is also assumed that if the y^+ value near the wall satisfies the limit of $y^+ < 4$, this operating regime is in the so-called diffusion-dominating regime. Here, the particles are dominated by turbulent and Brownian diffusion in the vicinity of the wall. By combining this assumption and the valid Stokes-Cunningham law, the Brownian motion can be included in the particle influencing physical models.

6.2 Particle implementation

The particles are implemented and injected into the fluid flowing using the Discrete Phase Model (DPM) in Ansys Fluent. However, before the implementation of particles, the Stokes number must be calculated to verify that the assumption of one-way coupling holds. It is calculated in MATLAB (see appendix B) using the equation presented in section 4.3. By investigation, it is evident that the Stokes number are inversely dependent of the particle diameter. Hence, the magnitude of the Stokes number decreases with a decreasing particle diameter.

Consequently, the evaluation is limited to the largest particle size of 100 nm. If $Stk << 1$ for the 100 nm particles, then it will hold for the smaller particles as well. Therefore, the entity is evaluated and calculated at the different pressure regimes represented by the different sections.

Orifice	Stk
1 to 2	0.0232
5 to 6	0.0281
7 to 8	0.0206

Table 6.1: Representation of the Stokes number at the different pressure regimes given a particle diameter of 100 nm

By observing the resulting Stokes number in table 6.1 the assumption of one-way coupling holds (Stk « 1). The one-way coupling with the flow can be enabled, resulting in no interaction from the particle on the flow. The particles are simulated as moving mass points, by selecting the particle type as inert. Each particle stream is calculated independently and represents a larger number of particles following the same trajectory. Furthermore, the particles are injected from the inlet surface, where the option of randomizing the starting points are enabled. This is done to adjust the number of particle trajectories injected into the flow. However, the number of particle streams tracked are significantly less than the actual number of particles dispersed in the IDDP-1 experimental test. The simulation is therefore reduced to quantifying the number of particle trajectories that escape through the outlet of the domain, and to investigate the accumulation of particles on the walls. As noted in the introduction, a variation of particle diameters of 1, 10 and 100 nm are implemented.

6.3 Numerical schemes and time steps

The Lagrangian particle tracking have to solved numerically. Contrary to the continuous fluid flow which is expressed by partial differential equations (PDE), the physics of the DPM is described by ordinary differential equations (ODE). Consequently, the DPM must use its own numerical scheme, which deviates from the other numerics used in Ansys. There are multiple numerical schemes of the DPM that can be applied to the simulation, and the reader is referred to the Ansys theory guide for a thorough explanation and derivation of the different alternatives [17].

Stordal introduced two of these, the trapezoidal and analytical numerical scheme. The trapezoidal scheme is the most accurate, but yields a larger computational time than the analytical, which uses an analytical integration. However, as described by Stordal, the relative error of the trapezoidal scheme is of much smaller magnitude than the analytical scheme as illustrated in figure 6.1. Therefore, it is desirable to use the trapezoidal scheme to obtain a reasonable solution of the DPM.

For the smaller particles, namely $d_p = 10$ nm and $d_p = 1$ nm, it is observed that the time step of the trapezoidal scheme is not sufficient to cover the entire particle trajectory through the domain. This is a result of that the trapezoidal time step is dependent of the particles

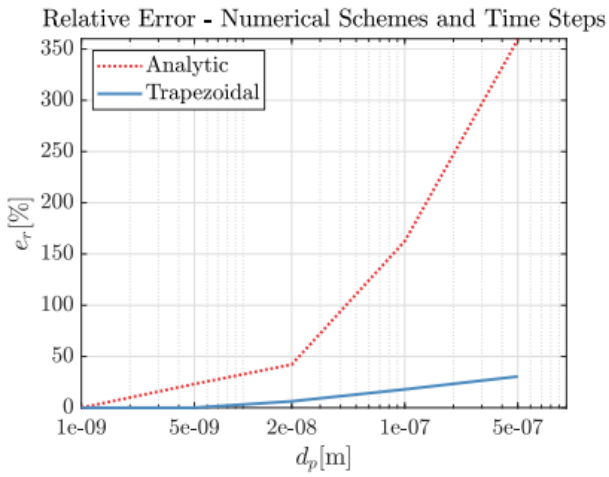

Figure 6.1: The relative error of the analytic and trapezoidal schemes based on the trapezoidal scheme with restricted time step of $\Delta t = \tau_p/2$ fetched from Stordal [3]

size, as described by Stordal [3]. Hence, as the particle size decreases, the scheme time step decreases. To prevent this phenomenon of arising the particle time step have to be controlled by implementing an UDF. Another option is to assume that for the smaller particles, the error of the analytical scheme is sufficiently small and apply this numerical scheme. This can be done since the time step of the analytical scheme is not particle size dependant, but dependant of the eddy time scale. The time step of the analytical scheme is set to $\tau_e/100$, with $\tau_e \approx 10^{-4}$.

Consequently, the trapezoidal scheme is employed for the particle size of 100 nm, whereas the analytical scheme is employed for 10 and 1 nm. In this matter, the computational time is decreased for the simulation of the smaller particles, and the particle trajectories are completed by excluding the insufficient time step of the trapezoidal method.

6.4 Tracking parameters

The tracking parameters of the particle trajectories have to be determined. The default value for a steady state one-way coupling yields a maximum number of steps of 50 000, with a specified step length factor of 5. When the maximum number of steps exceeds 50 000 and the particle is still circulating in the domain or the trajectory have encountered a low velocity domain, it is set as incomplete [17].

In addition, the high-resolution tracking is enabled. This feature applies a decomposition of all the computational cells into tetrahedrons (subtets) and tracks the particles through these subtets. This option provides a more robust tracking algorithm and improved variable interpolation. The variable interpolation is called barycentric interpolation, and it is used to obtain the flow solution (such as, velocity and temperature) at the particle position. When combined with high-resolution tracking, the barycentric interpolation provides improved accuracy and robustness and reduces the dependency on parallel partitioning. This interpolation is automatically enabled by Fluent [17].

6.5 Particle injection

1000 particles are injected at the surface inlet. For an even better statistical overview of the simulation it would be desirable to inject at least 10000 particles. However, this increases the computational time with a significant margin, resulting in a gigantic response time of the Fluent application. Consequently, the injection of 10000 particles must be aborted and an increased error have to be accounted for.

The particles injected are silica particles, and the silica properties are collected from Bergman et al. [30] presented in table 6.2

Properties	Values
ρ_p	2160 kg/m^3
c_p	44 J/kgK

Table 6.2: Properties of the silica particle

The point properties of the silica injection have to be determined as well. The velocity of the particles injected are set equal to the velocity of the fluid flow, and the total flow rate of the particles are determined by using the correlation of Fournier 4.2. This correlation is implemented and calculated using MATLAB, see appendix B.

6.6 Particle Forces and turbulent dispersion implementation

The forces acting on the particles were introduced in chapter 4, and the implementation of these models are presented below. Due to the incapability of implementing the UDF's by Stordal in a parallel processor and the significant increase in computational time by adding UDF's, the following in-built physical models of Fluent are employed:

- Saffman's lift force
- Erosion/Accretion
- Brownian motion
- Stokes-Cunningham drag law

By including these models, the general carrier effects and the accumulation of particles on the wall described by the accretion rate are accounted for.

The two first forces are enabled by hooking the models to the solution, whereas when activating the Brownian motion, the energy equation have to be enabled as introduced in subsection **??**. Hence, the inlet temperature and the temperature of the particles are set equally to each other and matching the inlet temperature of the respective orifices (Orifice 1, 5 and 7) given in table 5.2. The outlet temperature is set to the corresponding isenthalpic temperature calculated at the outlet (Orifice 2, 6 and 8) as shown in table 5.2. For the base case (section 1), this reads an inlet temperature of 723 K and an outlet temperature of 707.2764 K. A thermal boundary condition at the wall must be applied as well. As it is assumed that the simulation is isenthalpic and adiabatic the heat flux and heat generation are set to 0.

A special consideration has to be accounted for when activating the Stokes-Cunningham drag law as well. The Cunningham correction factor must be calculated, and this is done by

implementing equation 4.3 into MATLAB. The properties of the fluid at inlet conditions 5.2 and the silica particle 6.2 have to be included in the calculation to determine the Cunningham correction factor. This is evaluated for the different pressure stages and particle sizes. The resulting correction factor is presented in table 6.3.

		Particle diameter:	
Orifices:	1 nm	10 nm	100 nm
1 to 2	824,3678	82,9456	8,8433
5 to 6	777,0992	78,2189	8,3732
7 to 8	759,9646	76,5056	8,2029

Table 6.3: Representation of the Cunningham correction factor at the different orifices and particle diameters

6.7 Turbulent dispersion

The spurious drift of particles is linked to the turbulent dispersion through the discrete random walk model (DRW model). Consequently, by applying a DRW model, the turbulent dispersion can be accounted for in the domain. However, in the master thesis of Stordal it was concluded that the default DRW model of turbulent dispersion is not recommended for submicron particles. Based on the work of Longmire [31] and Mofakham and Ahmadi [32] an improved DRW model was employed in the master thesis of Stordal. However, likewise the other UDF's created by Longmire and Stordal, this improved DRW model could not be implemented in this master thesis since it does not compile for parallel processing. According to Stordal, several other authors have applied the default DRW model for submicron investigations, and Mofakham and Ahmadi showed that this model was susceptible to spurious drift of submicron particles as well [32]. However, it was also noted that this default DRW model produced a spurious drift of particles towards the wall, leading to a larger particle accumulation in the near-wall region and enhanced deposition.

In the absence of better options, the default DRW model is applied to enable stochastic tracking. Before enabling the DRW-model, the time scale constant is changed from 0.1 to 0.3 to account for the use of the RSM turbulence model [17].

6.8 Particle deposition

In the master thesis of Stordal, an UDF for tracking the number of particles colliding with the wall was created. It was assumed that when the particle-wall interaction occurred, the particle was deposited to the wall. Similar to the UDF by Stordal, Fluent has an in-built wall boundary condition denoted as the trapped boundary condition. For this instance, the trajectory calculations are terminated, and the fate of the particle is recorded as "trapped" when the particle-wall interaction occurs. However, neither the UDF nor the trapped boundary condition are applicable to the present study since the entire particle flow interacts with the back wall of the domain.

Therefore, the boundary condition at the wall is set to reflect and the particle deposition is monitored using the accretion rate in the Fluent application as described in section 4.3. The accretion rate can be understood as how many particle trajectories that interfere with the area of the cell face at the wall. As denoted in equation 4.5, the accretion is dependant of the mass flow rate of the particle and the area of the cell. However, in this present study the total mass flow rate of the particle is fixed. The mass flow rate of the particle is calculated by using the correlation of Fournier and the fluid flow rate. The calculation is shown in appendix B.

Furthermore, with a fixed particle flow rate, the accretion rate is dependant of the area of the cell face and the number of particles interfering with the cell face. At the wall, the face area is extremely small, due to the applied inflation layer, which will result in a very large accretion rate. Furthermore, to illustrate where the deposition will occur in the domain, the accretion rate is plotted as DPM contours. In addition, the accretion rate is monitored to obtain an overview of the deposition at different the three particle diameters (1, 10 and 100 nm). The three aforementioned sections of the cascade impactor are evaluated as well.

To assess the different pressure regimes, the properties of the fluid and particles have to be updated as aforementioned. To ensure a solution with a small relative error, the investigation regarding the different pressure regimes is implemented using the trapezoidal numerical scheme with the 100 nm particles injected into the domain. Simultaneously, this will simplify the investigation by restricting it to one size order.

In addition, it is desirable to compare the simulated silica scaling with the scaling rate collected in the IDDP-1 cascade test. Therefore, the accretion rate is quantified by integrating the accretion rate over the entire domain area. According to the Fluent theory guide, the integral on a surface is computed by summing the product of the facet area and the selected field variable facet value. In this study, the facet area represents the area of the domain, and the accretion rate is the field variable. This can be implemented since the accretion is denoted as kg/m^2s, yielding an integration over the area to obtain an accretion rate denoted as kg/s. For this instance, it is regarded easier to compare with other quantities, such as the fluid flow rate (kg/s).

The Schmidt number introduced in section 4.3 is also calculated in MATLAB to illustrate how the particle deposition varies with the particle diameter and the fluid properties yielded by the different pressure magnitudes.

To validate the resulting particle deposition from the present simulation, a comparison with the results from the IDDP-1 cascade test without filter is completed. These results are plotted and shown in figure 6.2, where the scaling of silica is plotted versus the pressure. The scaling rate was measured to be low above 80 bar but increases and is at its maximum between pressure of 40 to 50 bars and then decreases. The scale formed a dark dot opposite to the inlet where the steam impacted the orifice surface (see at the bottom of each orifice). Thick white coloured scale was also observed at the pressure around 50 bar.

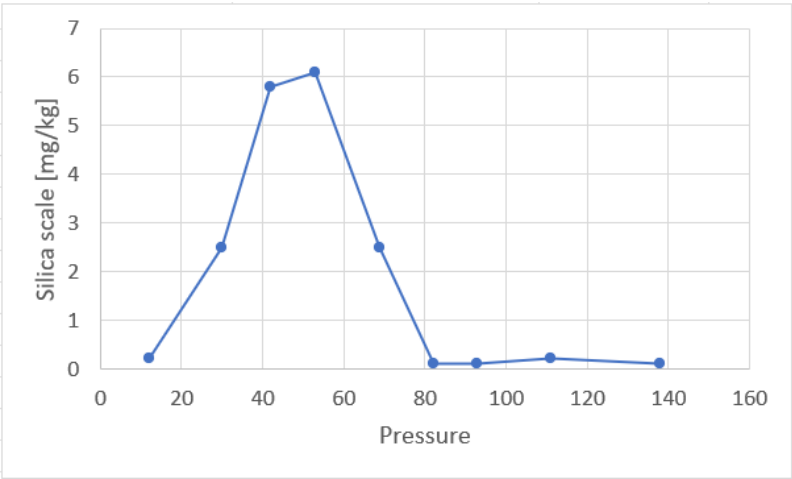

Figure 6.2: The deposition of silica from superheated steam

Figure 6.3: The scaling of silica on the different orifices in the experiment 1 of the IDDP cascade test

Chapter 7

Results and discussion

In the following chapter the resulting flow characteristics of the flow simulation is illustrated and discussed. Once the flow simulation is set, the particles are injected, and the latter is reviewed and discussed.

7.1 Flow simulation

The flow is simulated for the given geometry described in section 5.2, by applying the flow and boundary conditions introduced in section 5.5. The three different sections of the cascade impact test are evaluated. To verify that the pressure range is satisfactory good, the operating pressure is compared to the ones obtained in the experimental results of the IDDP-1 experiment. The pressure of the first section is represented through the pressure contour shown in figure 7.1.

Through inspection of figure 7.1, the outlet pressure can be verified to be around 111 bar, whereas the inlet pressure is of a lower pressure than for the experimental results. The pressure at the inlet is coloured yellow, yielding an inlet pressure of around 120 bar.

To obtain an overview of the pressure magnitude, the total pressure was measured at the inlet (in) of the case, at the pressure maxima on the back wall represented with the red color in the pressure contour 7.1 (innwall), at the middle of the back wall (midwall) and at the outlet of the case (out). An illustration of where the measurement points are located in the domain is shown in figure 7.2. The values are listed in table 7.1, and it is therefore evident why the total pressure at the midwall is not visible in figure 7.1, since it is almost identical to the outlet pressure.

Position:	Press [bar]
In	121.838
Inn wall	121.557
Mid wall	116.990
Out	116.997

Table 7.1: The pressure at the different points in the domain

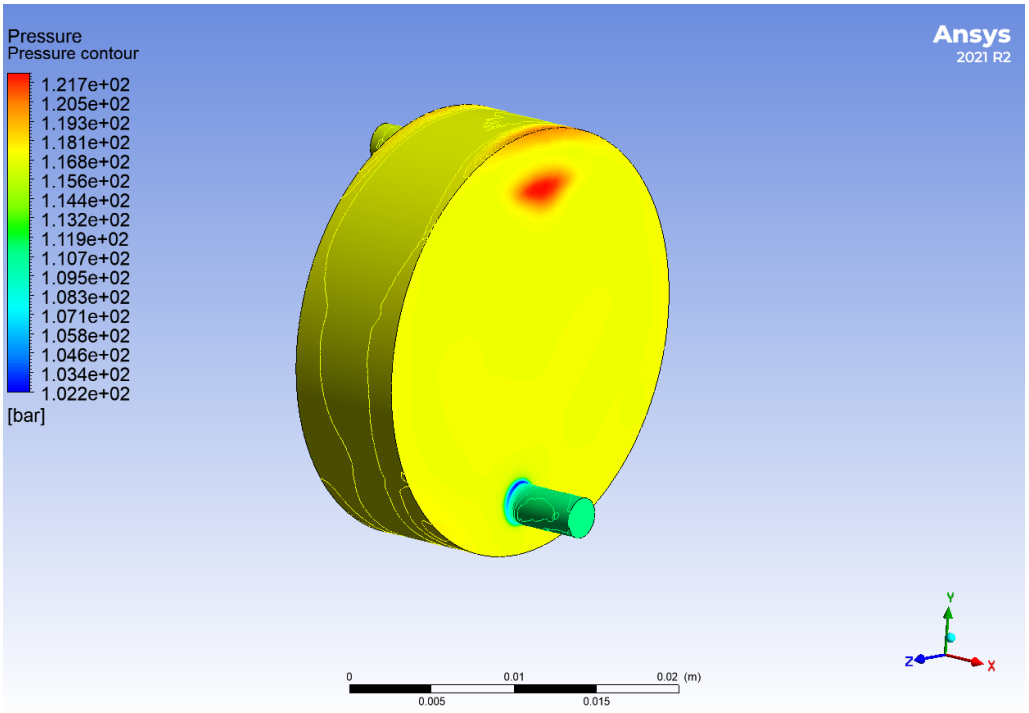

Figure 7.1: Illustration of the pressure contour of the fluid flow between the inlet and orifice 2

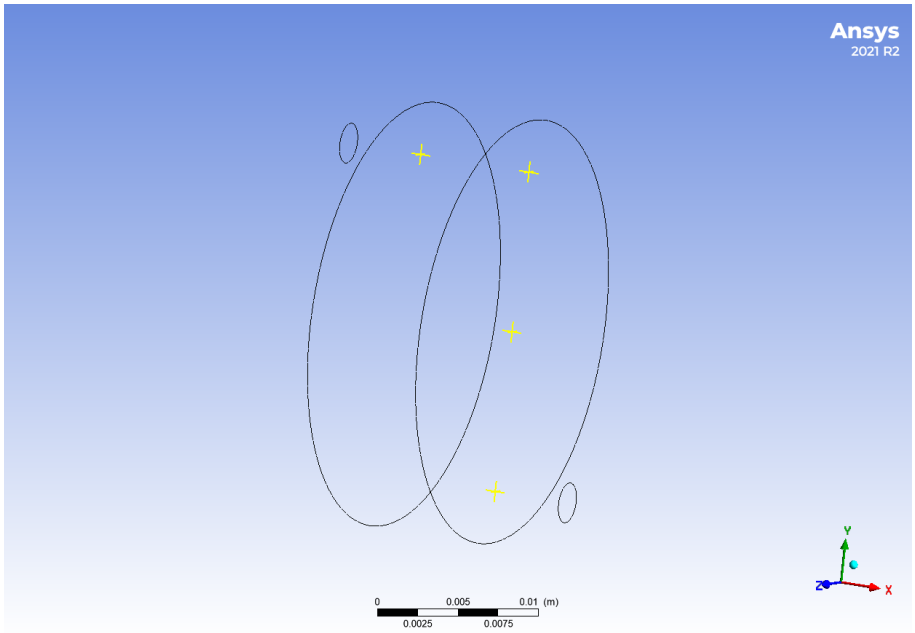

Figure 7.2: Illustration of the measuring points

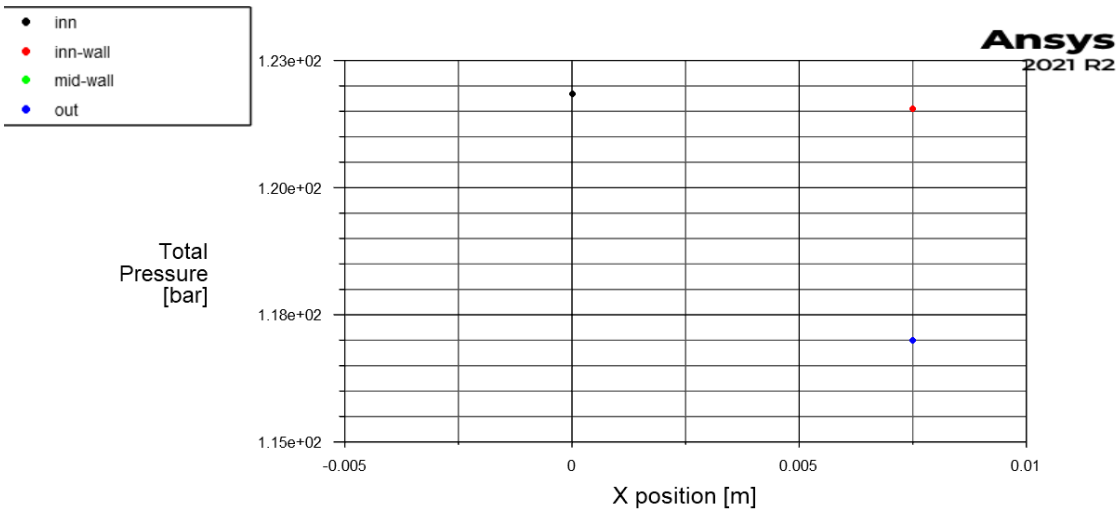

Figure 7.3: The pressure contours of the fluid flow between the inlet and orifice 2

The pressure contour (figure 7.1) and the corresponding pressure magnitudes at the different measurement points (table 7.1) are compared. Here, it can be observed that the simulated pressure drop is of a smaller magnitude than the one measured in the IDDP-1 cascade test. By comparing the pressure in orifice 1 from table 5.1, with the pressure at the inlet in table 7.1, it can be seen that the pressure deviates with approximately 10 bars. This is approximately 10 % of the total pressure, which is a significant difference. The reasons behind this can be explained through several factors. In the simulation it is assumed that the process is isenthalpic and adiabatic. Hence, there are no exchange of heat from the process to the surroundings. In the IDDP experiment however, some losses to the surroundings will occur and this will affect the pressure drop as well. In essence, the pressure drop will increase when heat will be released to the surroundings. Other losses can be characterized by losses occurring in the components due to leakage, for instance at the orifices placed at the inlet and outlet of the domain. However, in the simulation, the geometry is designed as an enclosed model, and leakage will not occur.

The velocity vectors of the fluid flow are also plotted and illustrated in figure 7.4. Here, it is illustrated that the entire flow enters the case with a high velocity and collides with the back wall. Afterwards, the flow is circulating in the case, before it exits, and the flow reaches its velocity magnitude. Since the flow is pressure driven, the velocity increases suddenly at the outlet where the flow enters a lower pressure region, and the properties will change accordingly. The velocity magnitude can be considered quite high at this maximum, but this can be explained due to the rapid change in area of the domain at the exit.

Likewise the pressure magnitude, the velocity magnitude is evaluated at the measuring points illustrated in figure 7.2. Since the measuring point is placed in the middle of the outlet, an approximation of the mean velocity in and out of the case is evaluated. Through discussions an adequate verification method when evaluating a turbulent flow, the velocity at the inlet (u_{in}) should be approximately 1.25 times the velocity at the outlet ($1.25 \cdot u_{out}$). This can be verified by examining figure 7.5, where $u_{in} = 145.252$ and $u_{out} = 113.068$ and $u_{out} \cdot 1.25 = 141.335$.

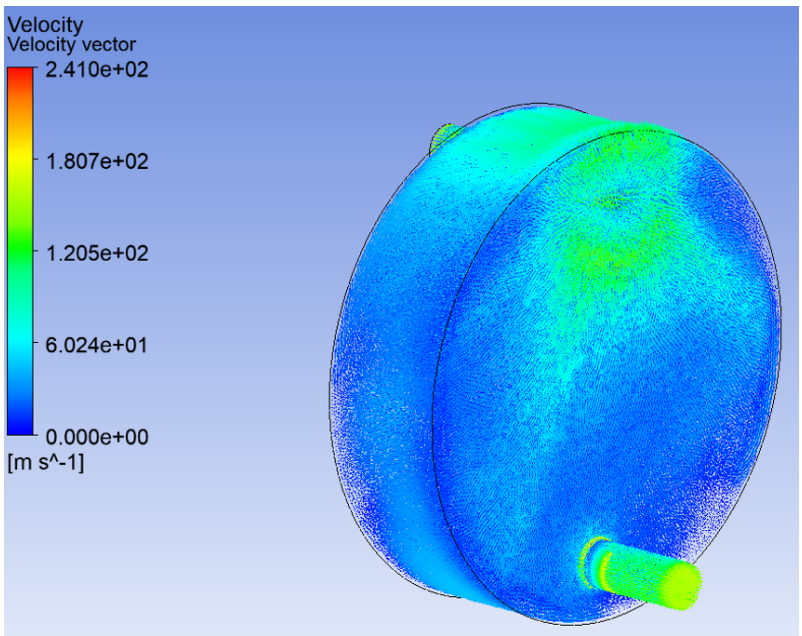

Figure 7.4: The velocity vectors of the fluid flow between the inlet and orifice 2

In addition, the no slip boundary condition is verified, yielding zero velocity at the mid- and in-wall.

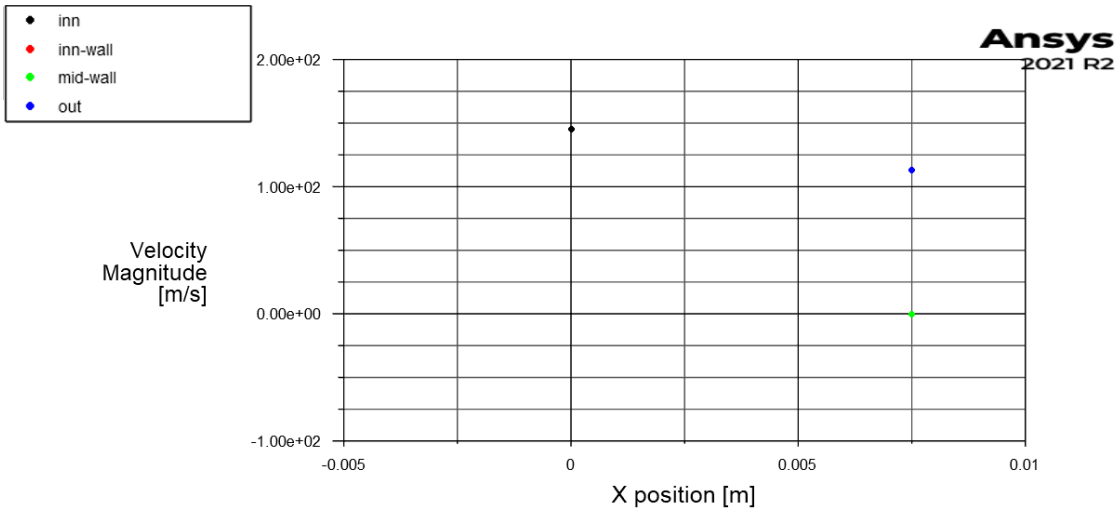

Figure 7.5: The velocity magnitude at the given measurement points

7.2 Particle simulation

7.2.1 Particle trajectories

Before injecting the particles into the fluid flow, the energy equation must be enabled in order to include the Brownian motion. Another boundary condition regarding the inlet and particle temperature is therefore imposed. However, since the operating condition is a one way coupling, and the heat flux applied to the wall is set to 0 there is no significant change in the pressure contour after particle injection (see figure A.1 in the appendix A). When assuming a on way coupling, the particles should follow the fluid flow. Hence, to illustrate how the particle trajectories will move along the flow the streamlines of 50 particle trajectories are plotted and illustrated in figure 7.6.

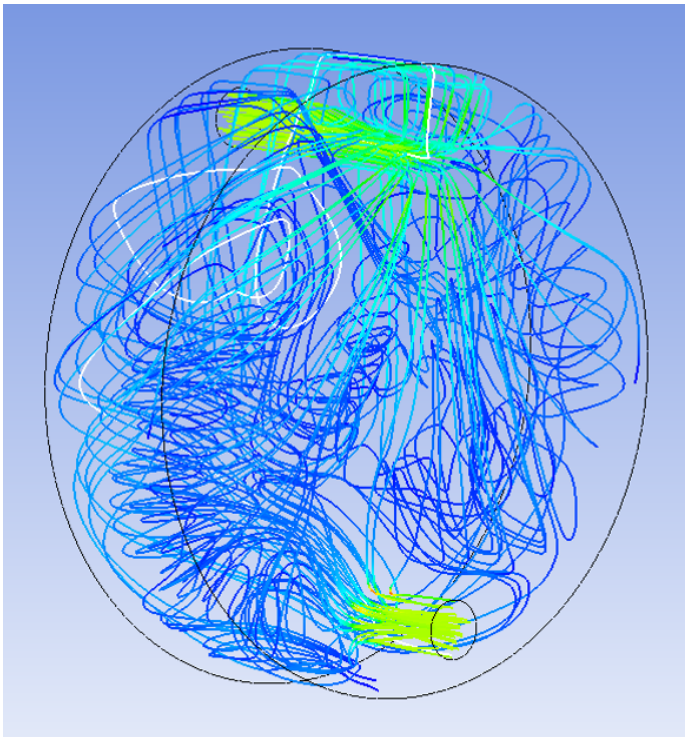

Figure 7.6: The streamlines of the fluid flow

Here, it is discovered that some of the particles are moving along the back wall down to the inlet, some are circulating over the inlet stream and back to the inlet wall, whereas others are experiencing a significant swirl of the fluid flow and are set as incomplete/deposited. To evaluate how the particles are influenced by the fluid flow the Schmidt number is calculated for the different sections and particle diameters. The results are shown in table 7.2, and by investigating equation 4.6 and the results it is evident that the Schmidt number decreases with a decreasing particle size. It is also at its lowest when the operating pressure is at its highest. Ergo, when the particles are at its smallest and the pressure is at its highest, the probability of deposition will be higher in this regime.

	Particle diameter:		
Orifices:	1 nm	10 nm	100 nm
1 to 2	0,0171	1,6977	159,2384
5 to 6	0,0324	3,2227	301,0525
7 to 8	0,0543	5,3962	503,2863

Table 7.2: The Schmidt number at the different sections and particle diameters

As described in the introduction, the deposition of particles is evaluated for three different particle sizes, 1, 10 and 100 nm respectively. Since the stochastic tracking is enabled, the particle trajectory can vary from one simulation to another. Therefore, several simulations should be performed, but due to a restrictive time schedule, it was limited to only three simulations per each particle size. Henceforth, the results must be carefully evaluated, and the resulting files are appended in the sample report in the Fluent application. However, it is noted that only three simulations for each particle size are not enough for a correct quantitative representation of the results, but due to a lack of time this will hold for a somewhat qualitative result. Nevertheless, the results are summarized below with the emphasis on the particle deposition:

For the largest particle size at 100 nm, the trapezoidal numerical scheme is employed. Hence, the most accurate solution will be obtained, ref. section 6.3. Of the 1000 injected particles, 30 particles are set to incomplete. When set to incomplete, the maximum number of time steps has been exceeded, and it can be assumed that these particles are circulating in the domain or have encountered a low velocity domain. This yields a probable particle deposition of these 30 particles. The particle residence time of the 100 nm particles is plotted and illustrated in figure 7.7, and the incomplete particle with the largest residence time is presented in figure 7.8. This particle hits the wall several times and encounters a swirling velocity region. Therefore, the assumption of particle deposition can be assumed valid.

The second evaluation regards the particle size of 10 nm. Firstly, the trapezoidal scheme was used, but it became evident that the time step of the simulation was not covering the entire particle trajectory, setting the majority of the particles to incomplete (600 of 1000). However, it is desirable to use the trapezoidal scheme to prevent the significant increase in relative error (see figure 6.1), so the maximum number of time step was increased from 50 000 to 100 000. However, the change of residence time was barely noticeable, making an increase in maximum number of time step to 200 000 necessary. Unfortunately, this resulted in an enormous computational time, making it impossible to carry out the simulation in a reasonable amount of time. Therefore, the numerical scheme was changed to the analytical, since the time step of the analytical scheme is not particle size dependant (see section 6.3). Now, all the particles were completed on the expense of the accuracy of the simulation, but an overview of the particle deposition regarding the accretion rate is obtained.

Following the implementation of the analytical scheme, the increased numerical time step is verified by observing the maximum total residence time. The magnitude of the residence time has increased to approximately 4.6e-2 s versus the residence time of the trapezoidal scheme at 2.8e-2 s. A possible disadvantage of this criterion can be that the particles encountering swirling and low velocity domains are followed during a longer time span resulting in a

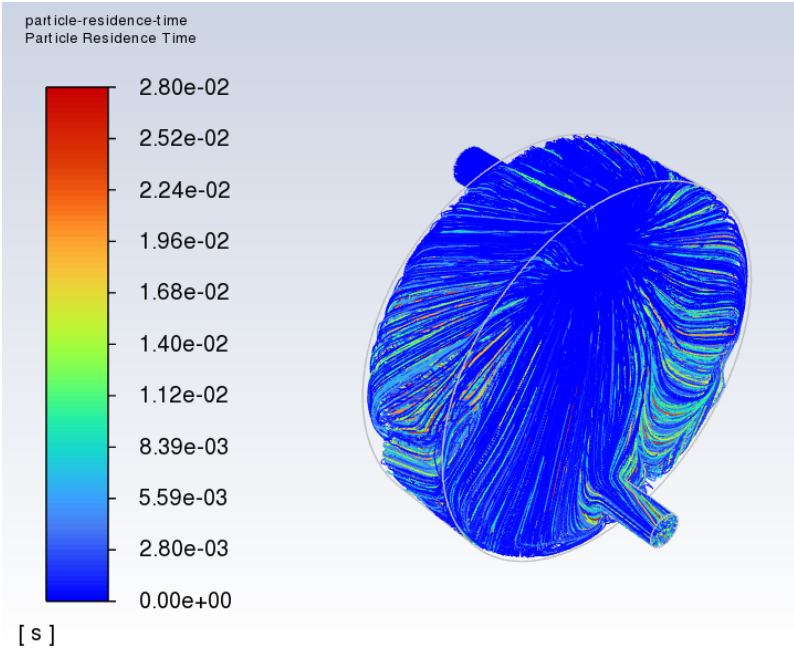

Figure 7.7: The residence time of the 100 nm particles

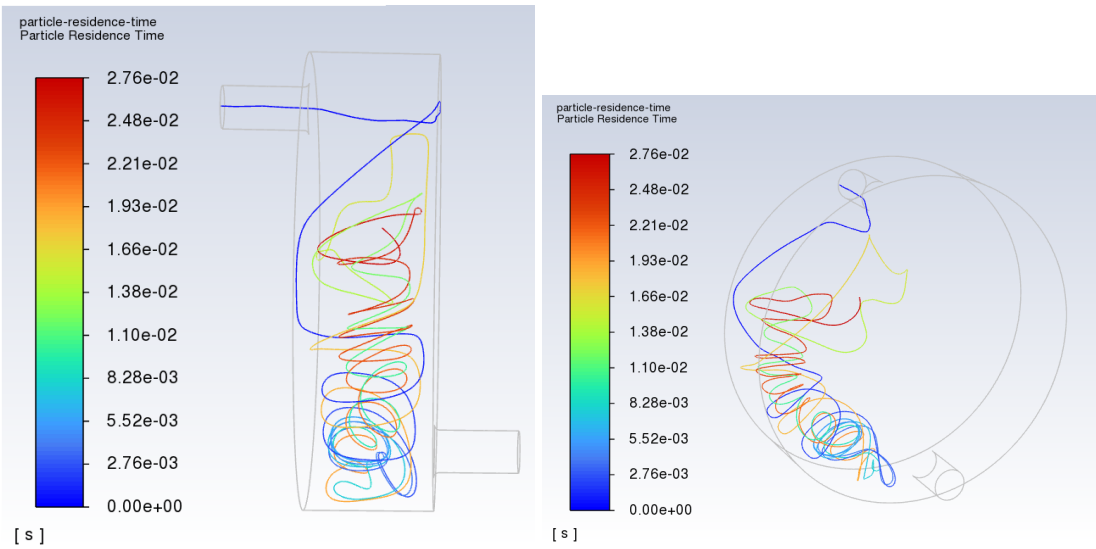

Figure 7.8: Illustration of the particle trajectory of the incomplete particle with the longest residence time

particle escape, even though they probably should have been set to incomplete and regarded as deposited. Some of these particles are also hitting the wall several times, which could also lead to particle deposition. The reader is referred to the appendix A for graphical illustrations

of the particle trajectories of the 10 nm particle injection and of the particle with the longest residence time. By investigation of these figures (figure A.2, A.3 and A.4), the aforementioned discussion is supported.

It is previously noted that when the particle size decreases, the particles are scarcely influenced by the viscosity of the fluid and are in equilibrium with the carrier fluid. This can be verified through the Schmidt number 4.6. Consequently, the number of deposited particles should increase with a decreasing particle size. However, due to the increasing time step, all of these particles are escaping the domain.

A similar phenomenon, is uncovered when the 1 nm particles are injected into the domain. Likewise the 10 nm particles, the maximal particle residence time is set to approximately 4.5e-2 s, and all the particles escape the domain (see appendix A for illustration of the particle trajectories).

7.2.2 Particle velocities

The particles are injected with the same velocity as the fluid flow, as it is assumed that the particles are in an equilibrium with the carrier fluid. This is also verified through table 6.1, where Stk « 1 for the 100 nm particles for all instances. As described in section 4.3, the Stokes number decreases with a decrease in particle size. It can be concluded that as the particle size decreases it tends to be more influenced by the carrier fluid. This is evident when investigating the particle velocity of the respective particle sizes, as the magnitude of the particle velocity increases when the particle diameter decreases from 100 nm to 1 nm, with a value of 217, 250 and 1000 m/s respectively. By comparing the maximum velocity of the fluid flow illustrated with the velocity vectors in figure 7.4, it is observed some abnormalities regarding the smaller particles. The magnitude of the 10 nm particle exceeds the maximal fluid velocity with 9 m/s. However, this can be regarded as satisfactory since it is only a relative error of 3.6 %.

On the contrary, the major error occurs for the 1 nm particle, where the maximal particle velocity of 1000 m/s is significantly higher than 241 m/s of the fluid flow. Through investigation this occurs in a local point in the flow, but when there are no instances of such a velocity leap in the fluid flow, this occurrence is regarded as physical impossible. Through discussions with the supervisors Bordvik and Næss, it was concluded that one possible reason for this phenomenon is that the particle size is of an order lower than the molecule size. Therefore, the Lagrangian particle tracking can be troublesome for the Fluent solver. However, it should be noted that when the particle sizes decrease, the particle Reynolds number will decrease. Subsequently, the drag force should have decreased, and the particles should have followed the fluid streamlines more easily, but this is not the case here. In this case, the particles follow the fluid flow too good, exceeding the maximal velocity. This special abnormality can be caused by some limitation in the Fluent software.

The reader is referred to the appendix A for the graphical illustration of the particle velocity magnitudes (figure A.6, A.7 and A.8).

7.2.3 Accretion rate

Since a tracking of deposited particles in the domain was not completed, the particle deposition is monitored through the accretion rate over the area of the domain and plotted as a

accretion contour. An overview of where the particle deposition will occur, is then obtained. The accretion rate of the three different particle sizes of 1, 10 and 100 nm are illustrated in figure 7.9, 7.10 and 7.11. By investigating the figures, it is made clear that some deposition of particles will occur at the back wall where the inlet flow hits, for all three cases. For the largest particle of 100 nm, some accretion will also occur at the "inlet wall", where the flow is circulating back after hitting the back wall as illustrated in the streamline figure 7.6. By comparing the three instances of accretion rate it is also made evident that when the particle size decreases the particle deposition is distributed more uniformly over the domain. These observations can be regarded as true, as the smaller particles are much more affected by the fluid flow and will follow the streamlines of the fluid for a longer time.

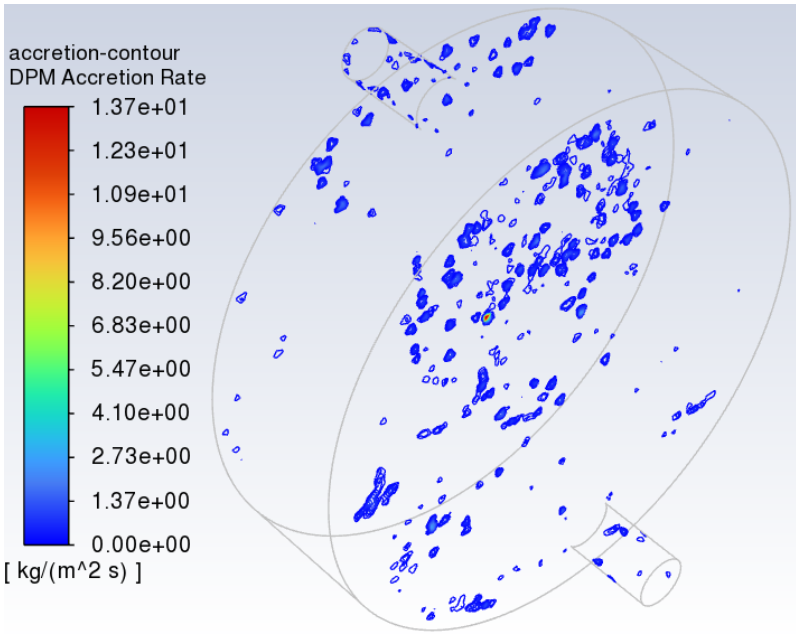

Figure 7.9: The accretion rate on the domain with a particle size of 100 nm

At the occurrence where several particle trajectories interfere with a particular cell face, the accretion rate will increase. Consequently, there will be instances where the accretion rate will be significantly high, as described in section 4.3. At the instances where the magnitude of the accretion contour appears (see red coloured in figure 7.9), the occurrence of particle deposition has its highest concentration. That is, several particle trajectories interfere with the wall at these points. The reason why the accretion magnitude is located at these positions can be explained through the swirling of the flow. It is discovered that a majority of the particles are swirling in these regions, which could lead to an increase in collisions with the wall. An example of this swirling flow is illustrated in figure A.4.

The actual size of the particles flowing in the steam in the IDDP-1 experiment can also be discussed and evaluated. Through inspection of the accretion contours, the 10 and 1 nm particles corresponds more to the scaling observed in the cascade test as illustrated in figure 6.3. Here it was observed a more uniformly deposition at the lower pressure rates, whereas it

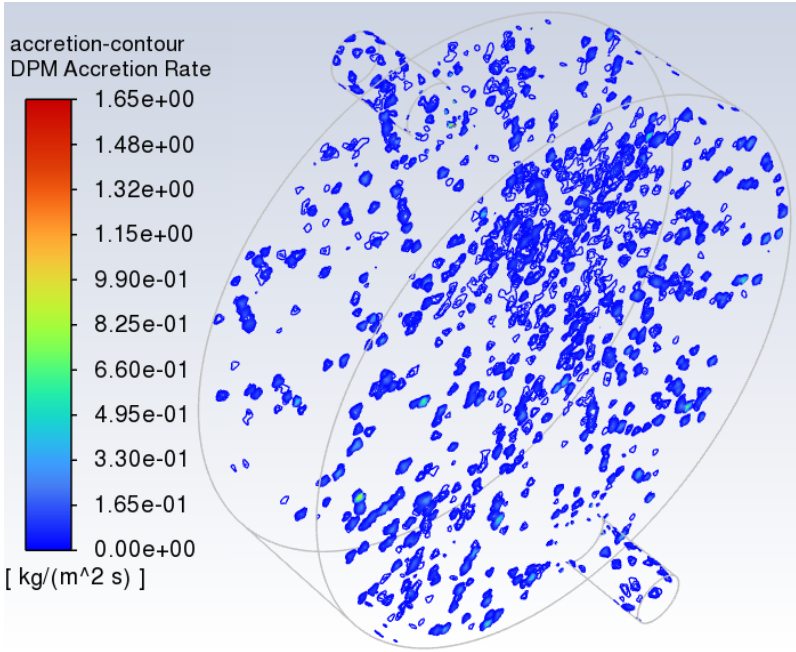

Figure 7.10: The accretion rate on the domain with a particle size of 10 nm

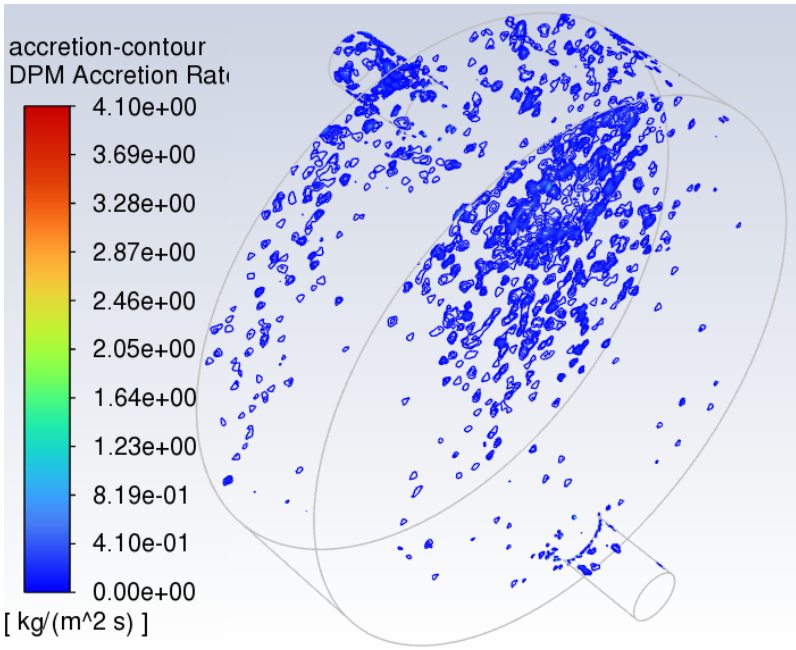

Figure 7.11: The accretion rate on the domain with a particle size of 1 nm

was more concentrated at

In addition to the variation of particle deposition at the different particle sizes, it is invest-

igated how the accretion rate varies over the aforementioned pressure ranges. The boundary conditions regarding temperature and pressure are updated, and the resulting pressure contours are illustrated in figure A.9 and **??** in appendix A for verification purposes. The particle velocities at the different pressure regimes are listed in appendix A as well (figure A.10 and A.11).

The investigation is restricted to the 100 nm particles, as introduced in the section 4.3. Hence, figure 7.9 illustrates the accretion rate at the first section. The accretion rate contour of the second (Orifice 5 to 6) and third (Orifice 7 to 8) section is illustrated in figure 7.12 and 7.13.

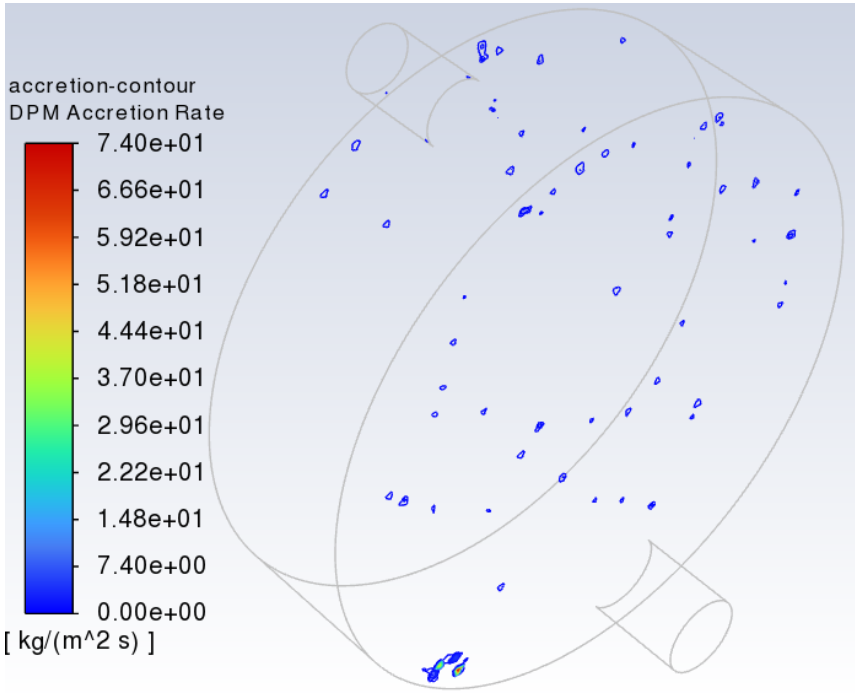

Figure 7.12: The accretion contour representing the particle deposition between orifice 5 and 6

Here, it is evident that the particle deposition is decreasing with the decrease in pressure, as the area coloured due to accretion decreases with the decreasing pressure. This observation deviates from the IDDP-1 cascade results, where the largest amount of silica scaling occurred at the second section (see figure 6.2 and 6.3). Some similarities are obtained, where it can be observed that the black dot on the back wall at the different sections in figure 6.3 can be illustrated as the accumulation of accretion contour in the same area in the simulation plots. As aforementioned, a more uniformly distribution the scaling occurs for the smaller particles. Therefore, the distribution of the particle deposition regarding the particle size of 10 nm can be regarded as similar to the IDDP-1 test results. By comparing with figure 6.3, it is evident that the distribution has similarities.

When evaluating the particle deposition at the pressure regimes, it should also be noted that the accretion rate is more concentrated at fewer locations when the pressure decreases.

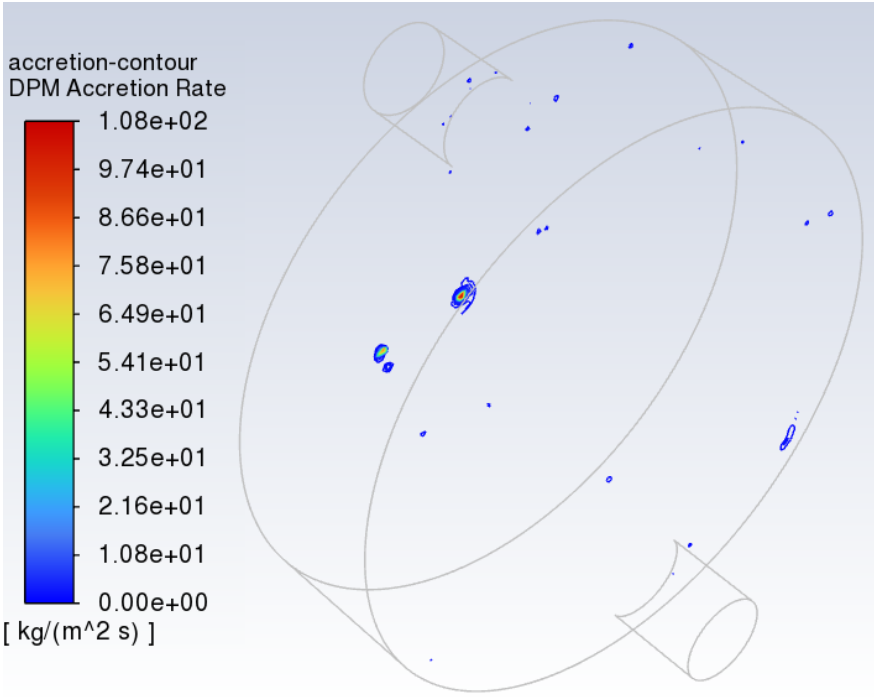

Figure 7.13: The accretion contour representing the particle deposition between orifice 7 and 8

This is verified by inspecting the increasing magnitude of the DPM Accretion rate in figure 7.9, 7.12 and 7.13, where accretion rate magnitude increases when the pressure decreases.

Consequently, the actual size of the particles flowing in the steam in the IDDP-1 experiment can be discussed and evaluated. Through inspection of the accretion contours, the 10 and 1 nm particles corresponds more to the scaling observed in the cascade test at the lower pressure sections, as illustrated in figure 6.3. Here it was observed a more uniformly deposition at the lower pressure rates, whereas it was more concentrated for the higher pressure rates (see for example at the second orifice). As a result, it can be assumed that for the higher pressure rate, the larger particles will be the ones dominating the particle deposition. This can be verified by comparing figure 7.9 and the second orifice in 6.3. Here only the black dot of silica scaling is visible, which can be seen in figure 7.9 as well. Henceforth, the smaller particles follow the fluid flow further down the cascade sections and are deposited more uniformly over the domain at the lower pressure rates.

In order to compare the magnitude of the accretion rate with the IDDP-1 results, a quantifying of the results is obtained by calculating the integral over the domain. The following results were obtained for the different particle sizes (table 7.3) and sections (table 7.4).

Particle size:	1	10	100
Integral $[kg/m^2s][m^2]$	1.3095e-05	1.1858e-05	2.6499e-05

Table 7.3: The accretion rate when injecting different particle sizes

Section:	1	2	3
Integral $[kg/m^2s][m^2]$	2.6499e-05	3.3386e-05	2.6702e-05

Table 7.4: The accretion rate at the different sections

By investigating these results, it can be seen that the total particle deposition over the domain increases with an increasing particle size. However, this observation is in dissent with the available theory through the Schmidt number. Here, conclusions were drawn that the possibility of particle deposition would increase with a decreasing particle size. This observation can be explained by the limitation of the accretion rate since it does not take any viscous contributions into account.

Through inspection of the particle deposition at the different pressure regimes it is observed that the total accretion over the domain follows the same trend as for the results of the IDDP-1 cascade impactor (see figure 6.2). The accretion is at its highest at section 2 (pressure around 50 bar), and lower at the two other sections.

To compare with the results from the IDDP-1 experiment, the deposition rate must be represented as mg solid matter over kg steam. The results in table 7.4 must be divided by the total fluid flow rate of 0.0355 kg/s, yielding the following results:

Section:	1	2	3
Simulated scaling [mg/kg]	746.4507	940.451	752.1690
Experiment scaling [mg/kg]	0.2	6.1	2.5

Table 7.5: The scaling at the different sections

In the IDDP-1 experiment the total solid matter collected was 17 mg per kg of steam. By comparing with the scaling in section 1, it observed that the simulated scaling is approximately 40 times larger at this section than the total solid matter collected in the cascade test.

In addition, it should be noted that it was discovered late in the master work that the correlation of Fournier, representing the concentration of the silica in the steam yielded a concentration lower than the one measured in the IDDP-1 test. Here, the concentration at the inlet was measured to 62 mg/kg, while the concentration using the Fournier correlation was calculated to 38.2892 mg/kg. By applying the measured concentration instead, the resulting silica scaling would have been even higher.

Consequently, it is determined that the accretion rate overestimates the deposition rate severely. This observation is verified through inspection of table 7.5 as well. This is probably a result of the limitation of the accretion rate since it tracks all the particles that interferes with the wall. However, it is not considered that if the velocity of the fluid is of a great magnitude, there will be no deposition of particles at the wall. Another reason of the overestimation of particle deposition can be caused by implementing the default DRW-model. As described in section 6.7, this model yields a spurious drift of particles towards the wall, resulting in enhanced particle deposition. Henceforth, further optimization of this numerical model is necessary to obtain a quantitative representation of the particle deposition.

Chapter 8

Conclusion

The objective of this thesis was met, namely the execution of numerical simulations of a cascade impactor. A numerical model representing the geometry of the cascade impactor was established in Ansys SpaceClaim and Ansys Meshing, and the fluid flow of a superheated and supercritical vapor vapour was implemented in the Ansys Fluent application. Subsequently the submicron particle deposition was studied with the Euler-Lagrangian approach. The respective properties of the fluid flow and particles were fetched from the theory and calculated using MATLAB.

As this thesis is a continuation of the work of Stordal, the UDF's created by Stordal were supposed to be implemented in this numerical model to account for the body forces on the particles. In addition, Stordal created an updated discrete random walk model (DRW model) of the particles as the default model in Fluent enhance particle deposition. However, these UDF's were not designed for parallel processing, and had to be aborted. Simplifications were made, and the body forces were implemented together with the default DRW model in fluent.

The particle deposition was monitored for three different particle sizes of 1, 10 and 100 nm respectively, using the in-built method in Fluent denoted as the accretion rate. Furthermore, to compare the deposition with the results from the cascade impactor in the IDDP-1 experimental test, three different sections with different pressure ranges (Outlet pressure of 111, 53 and 30 bar respeCtively) was investigated.

As a qualitative representation of the particle deposition some interesting aspects were observed. For the smaller particles the particle deposition is distributed more uniformly over the domain, whereas the larger particles are not nearly as prone to the sudden changes of the fluid flow. The deposition of the larger particles is therefore more concentrated at certain locations in the domain. The same phenomena of concentrated particle deposition were observed when the pressure decreased. By comparing with the results of the IDDP cascade test it can be concluded that the larger particles will be deposited at the higher pressure rates. Additionally, the more uniformly distributed particle deposition observed for the smaller particles matches the cascade results at the lower pressure rates. The particle distribution of the smaller particles is therefore regarded as more similar to the results of the experimental test for the lower pressure regions.

When attempting to quantify the accretion rate problems occurred, and it was concluded that the accretion rate is restrictive. The entity is only dependant of the mass flow rate of

the particle, the number of particles colliding with the wall and the area where the collision occurs. This parameter does not take any viscous contributions into account, and it deviates from the introduced Schmidt number, which identifies the possibility of particle deposition. According to the Schmidt number, the smaller particles have a greater possibility of particle deposition. After the simulations, the accretion rate yielded the total opposite results, with a greater particle deposition for the larger particles.

The accretion rate was compared with the scaling measured in the IDDP-1 experimental results. It was discovered that the simulated scaling in section 1 (Outlet pressure of 111 bar) exceeded the total actual scaling with a factor of about 40. It was that that together with the enhanced deposition rate of the default DRW-model, the accretion rate overestimates the particle deposition in the domain by a significant margin.

Chapter 9

Further work

It was concluded that the quantification method of particle deposition, namely the accretion rate overestimated the total particle deposition in the domain. Hence, this numerical model will benefit of an optimizing regarding the particle tracking and deposition. In the master thesis of Stordal, an improved model was imposed to enhance the accuracy of particle deposition and particle tracking [3]. However, this model was created only for serial processing, and the serial processor have been deprecated in the newer versions of Fluent. Hence, the following is recommended for further work

- Due to the inability of implementing the user defined functions (UDF's) created by Stordal to improve the particle modelling, it would be desirable to parallelize these UDF's. By doing so, the transport and deposition mechanisms of the diffusion-dominated submicron particles will be improved. This will also reduce the overestimation of particle deposition, and probably illustrate the deposition in a more correct matter.
- The ideal trapezoidal numerical scheme used to track the submicron particles utilize a time step which is particle dependant. Consequently, the time step of the smaller particles is exceeded before they have left the domain. Therefore, the use of the trapezoidal method is not adequate for the smaller particles, and the less desirable analytic method is employed. By creating an UDF to control the time step of the trapezoidal scheme, the scheme could be implemented for smaller particles as well. A possible solution could be to employ the time step dependency used by the analytical scheme, namely one thousand of the eddy time.
- The UDF imposed for the wall boundary condition to quantify the particle deposition by Stordal need to be optimized. The current UDF impose a particle as deposited when it hits the wall. However, for this numerical model all the particles hit the back wall after the inlet. The improved UDF should take the number of collisions with the wall into account. Say, a particle is regarded deposited after three or more collisions with the wall. Some of the particles are also experiencing a major swirl, leading to a significant increase in residence time. By taking the residence time of the particle into account in the UDF would be desirable as well, as it can be presumed that a particle is regarded as deposited when the residence time exceeds a particular residence time.
- Further investigations and validation of the numerical model.

Bibliography

[1] G. O. Fridleifson, H. Armannsson, K. Arnason, I. T. Bjarnason and G. Gislason, 'Feasibility study for IDDP deep drilling,' Tech. Rep. OS-2003/007, May 2003. [Online]. Available: https://orkustofnun.is/gogn/Skyrslur/OS-2003/OS-2003-007.pdf.

[2] S. N. Karlsdottir, K. R. Ragnarsdottir, I. O. Thorbjornsson and A. Einarsson, 'Corrosion testing in superheated geothermal steam in Iceland,' *Geothermics*, vol. 53, pp. 281–290, 2015, ISSN: 0375-6505. DOI: https://doi.org/10.1016/j.geothermics.2014.06.007. [Online]. Available: https://www.sciencedirect.com/science/article/pii/S0375650514000777.

[3] T. V. Stordal, 'Particle Deposition From Geothermal Supercritical Steam,' English, M.S. thesis, NTNU, Trondheim, Jun. 2021. [Online]. Available: https://ntnuopen.ntnu.no/ntnu-xmlui/handle/11250/2779976.

[4] B. F. Towler, 'Chapter 11 - Geothermal Energy,' in *The Future of Energy*, B. F. Towler, Ed., Boston: Academic Press, 2014, pp. 237–256, ISBN: 978-0-12-801027-3. DOI: https://doi.org/10.1016/B978-0-12-801027-3.00011-7. [Online]. Available: https://www.sciencedirect.com/science/article/pii/B9780128010273000117.

[5] G. of Iceland, *Energy*, 2017. [Online]. Available: https://www.government.is/topics/business-and-industry/energy/.

[6] D. B. v. d. Heuvel, E. Gunnlaugsson, I. Gunnarsson, T. M. Stawski, C. L. Peacock and L. G. Benning, 'Understanding amorphous silica scaling under well-constrained conditions inside geothermal pipelines,' *Geothermics*, vol. 76, pp. 231–241, 2018, ISSN: 0375-6505. DOI: https://doi.org/10.1016/j.geothermics.2018.07.006. [Online]. Available: https://www.sciencedirect.com/science/article/pii/S0375650517303796.

[7] L. F. Melo, T. R. Bott and C. A. Bernardo, 'Adhesion and removal of particles I,' in *Fouling science and technology*, vol. 145, Kluwer Academic Publishers, 1988, pp. 87–145, ISBN: 90-247-3729.

[8] I. Geosurvey, Mannvit, Kemía, I. C. Iceland, Verkís and Á. Einarsson, 'IDDP 1 Flow test 2010-2012,' Tech. Rep. LV-2013-050, Apr. 2013, p. 298.

[9] S. L. Nybu, 'Review of the intermolecular forces acting on solid particles in a steam,' English, Project thesis, NTNU, Trondheim, Dec. 2021.

[10] V. E. S. Paulsen, 'Deposition of silica particles in turbulent superheated steam,' English, M.S. thesis, NTNU, Trondheim, Jan. 2020. [Online]. Available: https://ntnuopen.ntnu.no/ntnu-xmlui/bitstream/handle/11250/2656752/no.ntnu%3Ainspera%3A50408330%3A38272637.pdf?sequence=1&isAllowed=y.

[11] H. Ohshima, 'Chapter 14: Theory of Colloid and Interfacial Electric Phenomena,' in *INTERFACE SCIENCE AND TECHNOLOGY*, vol. 12, 2006, ISBN: 978-0-12-370642-3. (visited on 19/11/2021).

[12] R. Caenn, H. C. H. Darley and G. R. Gray, 'Chapter 4 - Clay Mineralogy and the Colloid Chemistry of Drilling Fluids,' in *Composition and Properties of Drilling and Completion Fluids (Sixth Edition)*, R. Caenn, H. C. H. Darley and G. R. Gray, Eds., Sixth Edition, Boston: Gulf Professional Publishing, 2011, pp. 137–177, ISBN: 978-0-12-383858-2. DOI: https://doi.org/10.1016/B978-0-12-383858-2.00004-4. [Online]. Available: https://www.sciencedirect.com/science/article/pii/B9780123838582000044.

[13] T. Hao, 'Chapter 6 - Physics of electrorheological fluids,' in *Electrorheological Fluids*, ser. Studies in Interface Science, vol. 22, ISSN: 1383-7303, Elsevier, 2005, pp. 235–340. DOI: https://doi.org/10.1016/S1383-7303(05)80021-3. [Online]. Available: https://www.sciencedirect.com/science/article/pii/S1383730305800213.

[14] J. N. Israelachvili, 'Chapter 13 - Van der Waals Forces between Particles and Surfaces,' in *Intermolecular and Surface Forces (Third Edition)*, Third Edition, San Diego: Academic Press, 2011, pp. 253–289, ISBN: 978-0-12-375182-9. DOI: https://doi.org/10.1016/B978-0-12-375182-9.10013-2. [Online]. Available: https://www.sciencedirect.com/science/article/pii/B9780123751829100132.

[15] D. S. RIMAI and D. J. QUESNEL, 'Chapter 3 - Particle adhesion,' in *Adhesion Science and Engineering*, D. A. Dillard, A. V. Pocius and M. Chaudhury, Eds., Amsterdam: Elsevier Science B.V., 2002, pp. 139–191, ISBN: 978-0-444-51140-9. DOI: https://doi.org/10.1016/B978-044451140-9/50003-2. [Online]. Available: https://www.sciencedirect.com/science/article/pii/B9780444511409500032.

[16] L. Tian and G. Ahmadi, 'Particle deposition in turbulent duct flows—comparisons of different model predictions,' *Journal of Aerosol Science*, vol. 38, no. 4, pp. 377–397, 2007, ISSN: 0021-8502. DOI: https://doi.org/10.1016/j.jaerosci.2006.12.003. [Online]. Available: https://www.sciencedirect.com/science/article/pii/S002185020700002X.

[17] A. Fluent, *Ansys fluent theory guide*, 2022.

[18] K. Gersten, 'Hermann Schlichting and the Boundary-Layer Theory,' in *Hermann Schlichting – 100 Years*, R. Radespiel, C.-C. Rossow and B. W. Brinkmann, Eds., Berlin, Heidelberg: Springer Berlin Heidelberg, 2009, pp. 3–17, ISBN: 978-3-540-95998-4.

[19] te_rho, *Why is there no option for serial processing in Fluent 2020R1*, Question, Sep. 2020. [Online]. Available: https://forum.ansys.com/discussion/comment/90926#Comment_90926.

[20] R. O. Fournier and R. W. Potter, 'An equation correlating the solubility of quartz in water from 25° to 900°C at pressures up to 10,000 bars,' *Geochimica et Cosmochimica Acta*, vol. 46, no. 10, pp. 1969–1973, 1982, ISSN: 0016-7037. DOI: https://doi.org/10.1016/0016-7037(82)90135-1. [Online]. Available: https://www.sciencedirect.com/science/article/pii/0016703782901351.

[21] J. Simm, *Beach Management Manual*, ser. CIRIA report, 153. 1996, ISBN: 0-86017-438-7 978-0-86017-438-7.

[22] C. Gualtieri, A. Angeloudis, F. Bombardelli, S. Jha and T. Stoesser, 'On the Values for the Turbulent Schmidt Number in Environmental Flows,' *Fluids*, vol. 2, no. 2, 2017, ISSN: 2311-5521. DOI: 10.3390/fluids2020017. [Online]. Available: https://www.mdpi.com/2311-5521/2/2/17.

[23] G. H. Yeoh and J. Tu, 'Chapter 4 - Gas–Particle Flows,' in *Computational Techniques for Multiphase Flows*, G. H. Yeoh and J. Tu, Eds., Oxford: Butterworth-Heinemann, 2010, pp. 243–311, ISBN: 978-0-08-046733-7. DOI: https://doi.org/10.1016/B978-0-08-046733-7.00004-7. [Online]. Available: https://www.sciencedirect.com/science/article/pii/B9780080467337000047.

[24] wermac, *Dimensions Weld Neck Flanges Type 11 PN250*. [Online]. Available: https://www.wermac.org/din/dim_wn_flg_pn250.html (visited on 14/02/2022).

[25] A. Meshing, *Ansys meshing theory guide*, 2022.

[26] T. Avraham, *Know Thy Mesh – Mesh Quality – Part I*, English, Blog, Jan. 2019. [Online]. Available: https://cfdisrael.blog/2019/02/01/know-thy-mesh-mesh-quality-part-i/.

[27] Atgeirr, *What Are Good Orthogonal Quality Values?* Question, Mar. 2021. [Online]. Available: https://forum.ansys.com/discussion/25327/what-are-good-orthogonal-quality-values.

[28] L. Australia, *TIPS & TRICKS: INFLATION LAYER MESHING IN ANSYS*, 2013.

[29] Y. Cengel and J. Cimbala, *Fluid Mechanics Fundamentals and Applications*, 3rd ed. McGraw Hill, 2014.

[30] T. Bergman, T. Bergman, F. Incropera, D. DeWitt and A. Lavine, *Fundamentals of Heat and Mass Transfer*. Wiley, 2011, ISBN: 978-0-470-50197-9. [Online]. Available: https://books.google.no/books?id=vvyIoXEywMoC.

[31] P. Longmire, 'Computational fluid dynamics (CFD) simulations of aerosol in a U-shaped steam generator tube,' English, Doctoral Dissertation, Texas A&M University, 2007. [Online]. Available: http://oaktrust.library.tamu.edu/.

[32] A. A. Mofakham and G. Ahmadi, 'On random walk models for simulation of particle-laden turbulent flows,' *International Journal of Multiphase Flow*, vol. 122, p. 103 157, 2020, ISSN: 0301-9322. DOI: https://doi.org/10.1016/j.ijmultiphaseflow.2019.103157. [Online]. Available: https://www.sciencedirect.com/science/article/pii/S0301932219306366.

Appendix A

Resulting figures and plots

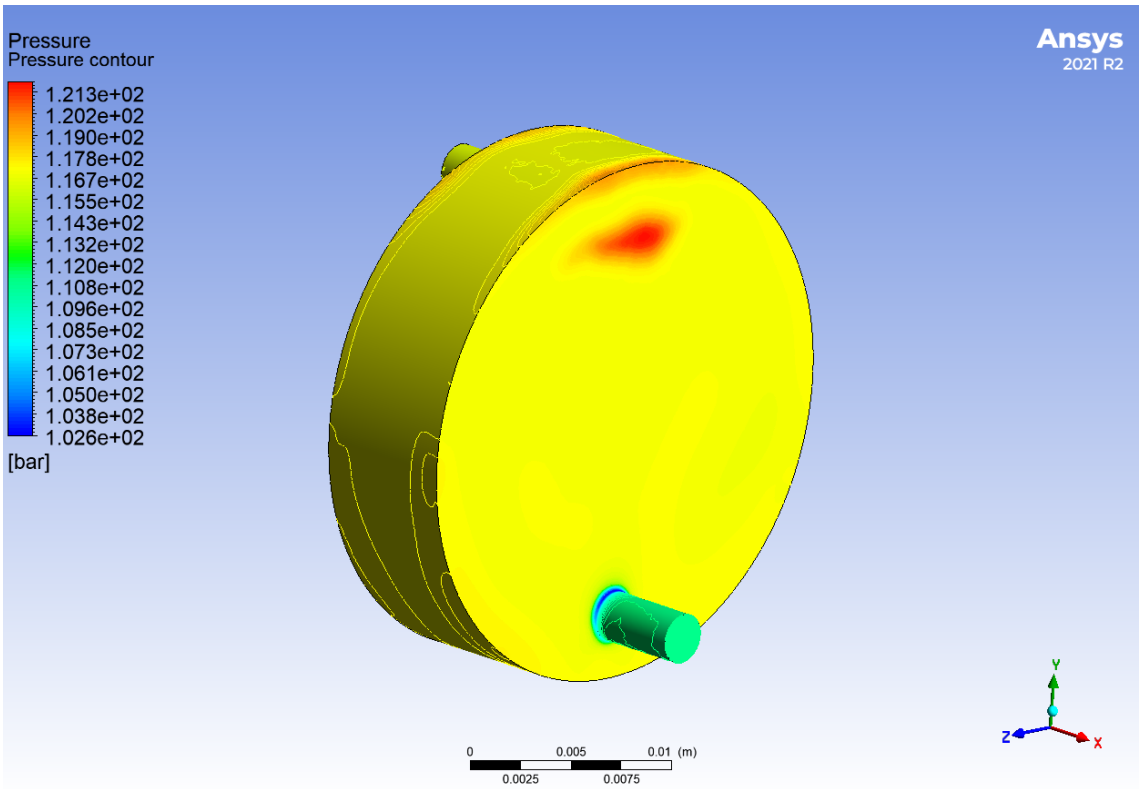

Figure A.1: The pressure contour of the fluid flow after injecting particles

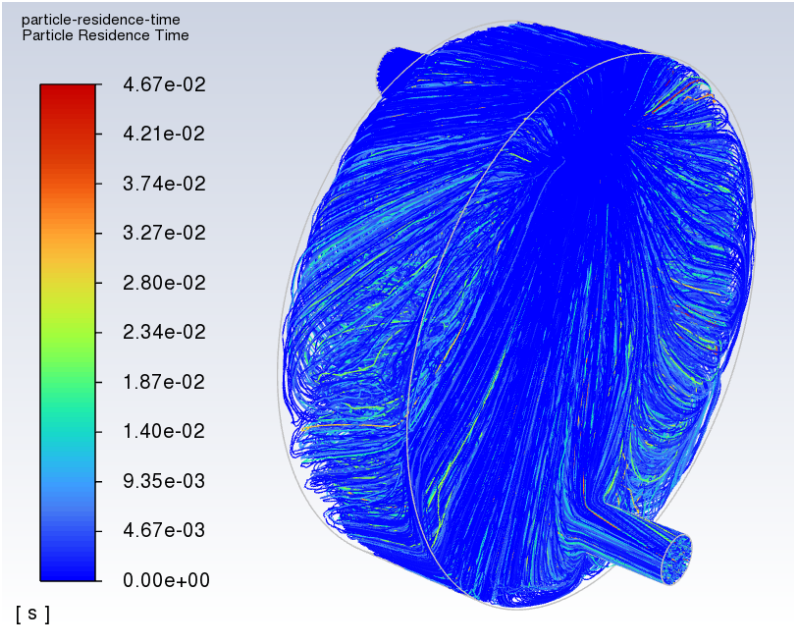

Figure A.2: The residence time of the 10 nm particles simulated with the analytical numerical scheme

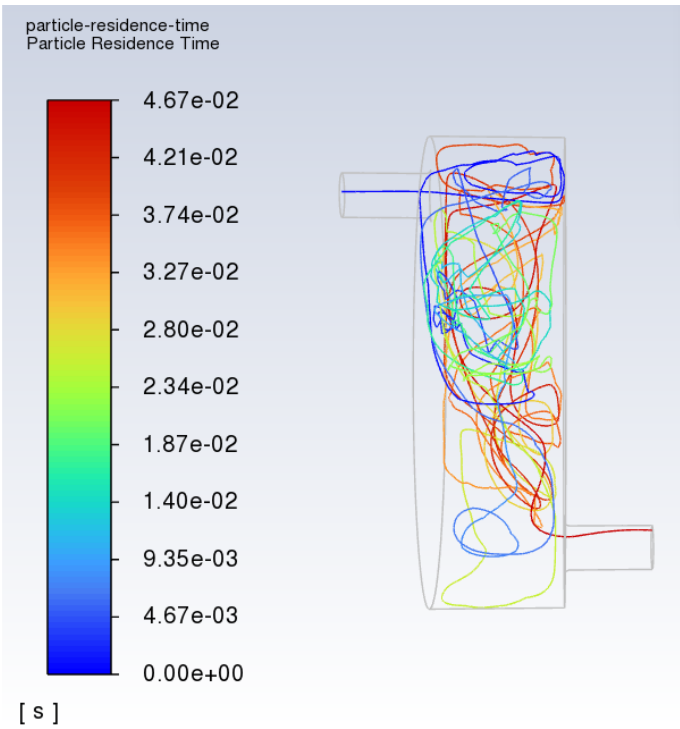

Figure A.3: The particle trajectory of the longest lasting 10 nm particle

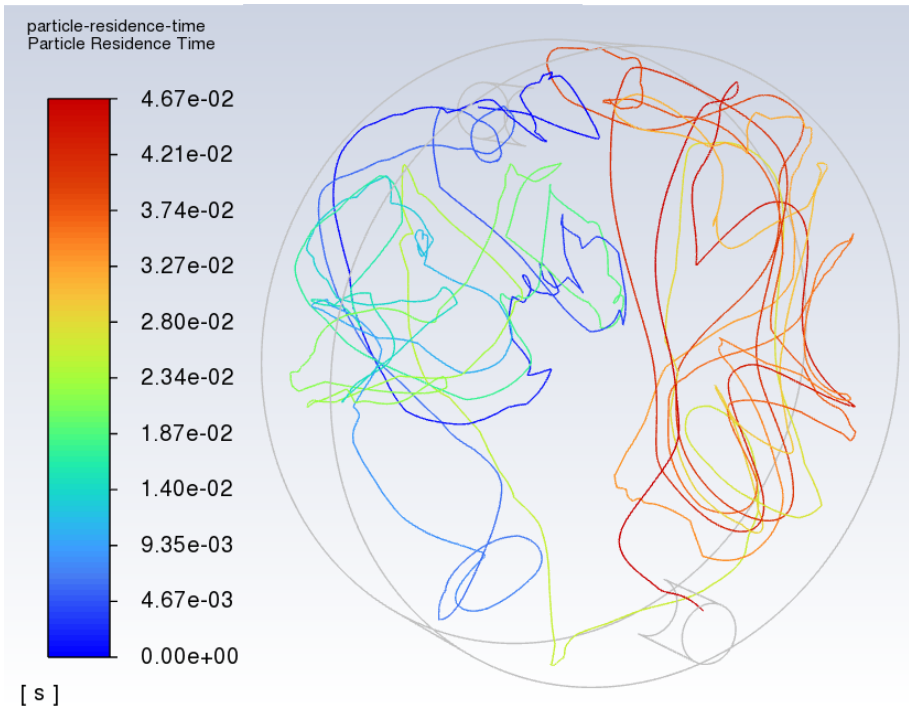

Figure A.4: The particle trajectory of the longest lasting 10 nm particle

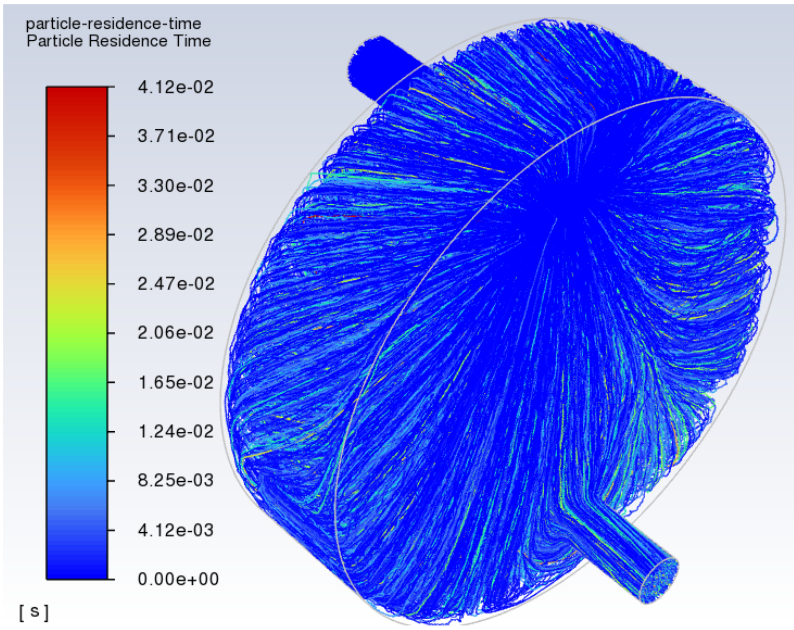

Figure A.5: The residence time of the 1 nm particles simulated with the analytical numerical scheme

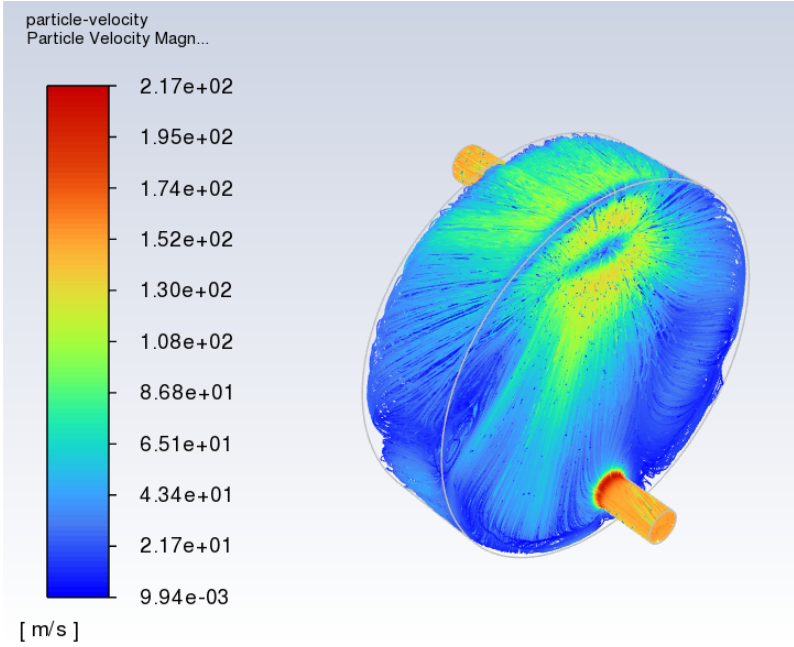

Figure A.6: The velocity magnitude of the 100 nm particle trajectories

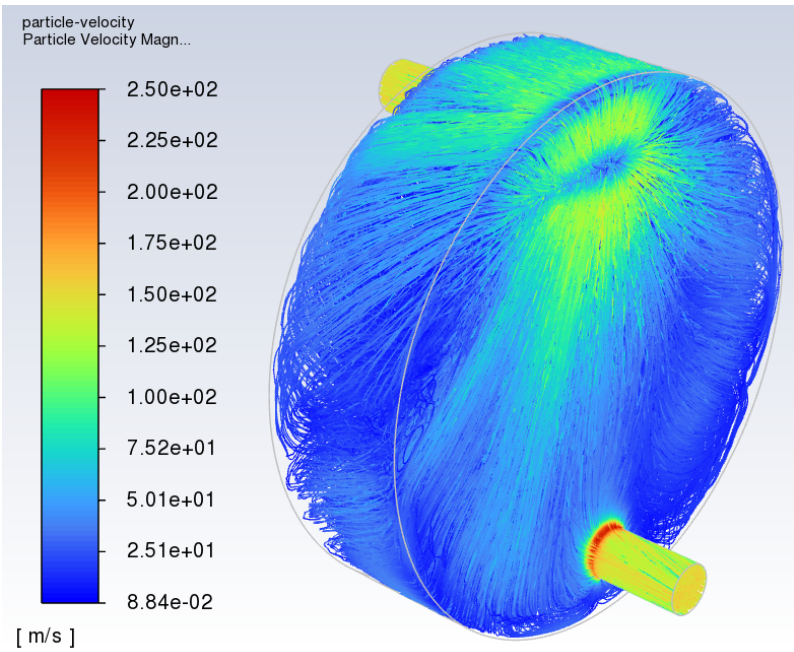

Figure A.7: The velocity magnitude of the 10 nm particle trajectories

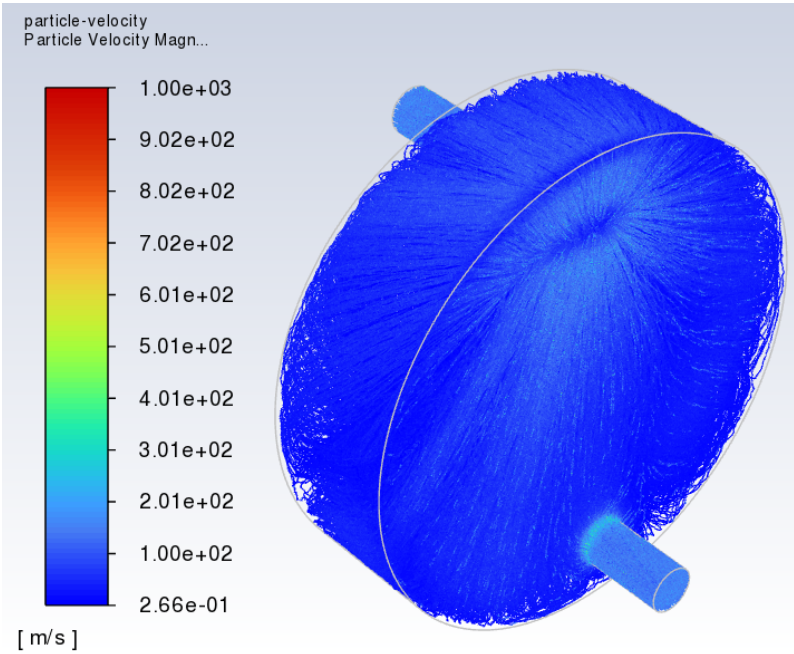

Figure A.8: The velocity magnitude of the 1 nm particle trajectories

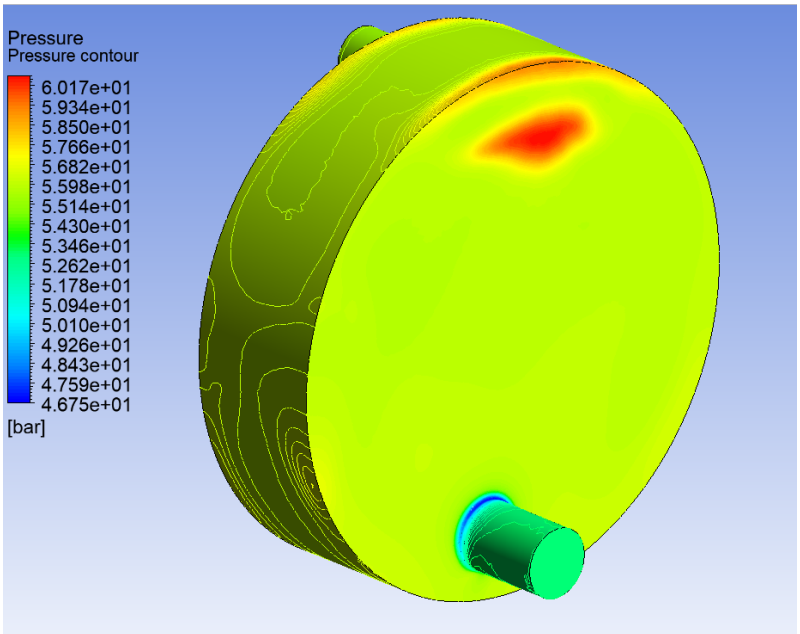

Figure A.9: The pressure contour of section two between orifice 5 and 6

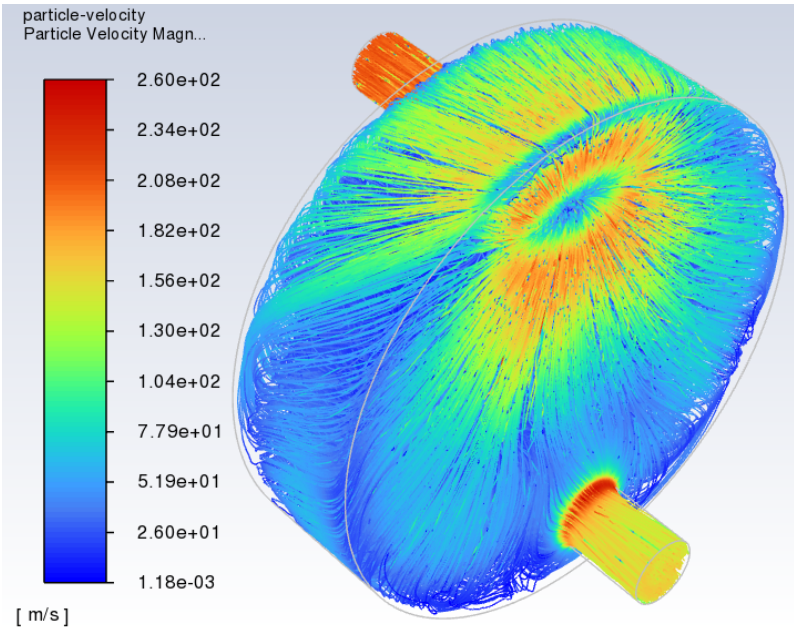

Figure A.10: The velocity magnitude of the particles in section two between orifice 5 and 6

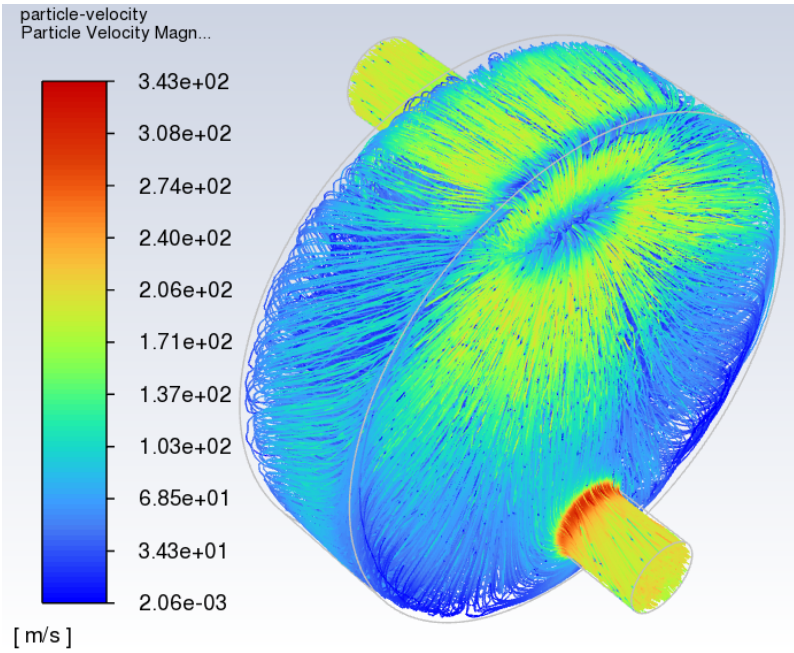

Figure A.11: The velocity magnitude of the particles in section three between orifice 7 and 8

Appendix B

Code listing

To calculate the different parameters in the calculation of the fluid flow field and particle modelling, the following Matlab code was utilized. It is based on the Matlab code by Paulsen [10]. When calculating the fluid properties at the different pressure ranges evaluated the properties at the different orifices or particle sizes are commented out. In the case listed below the properties of a 100 nm particle in the case of fluid flowing from the inlet to the second orifice is the one evaluated. However, the following code can easily be optimized to write out all of the desirable parameters for the different pressure ranges and particle sizes. The process would have been made easier and less time consuming instead of manually having to change the parameters for each computation.

```
%% Computation of various parameters based on the Matlab code of Paulsen


clear
close all
clc

% Fluid properties and dimensions updated for the present study

M = 18; % Molecular weight of steam [kg/kmol]
rho_f = 48.89986092; % fluid density [kg/m^3] inlet
%rho_f = 24.2724;    % orifice 5
%rho_f = 14.1738;   % orifice 7
rho_p = 2160; % silica colloid density
mu = 2.7005*10^-5;% Dynamic visc (u) inlet
%mu = 2.4683*10^-5; %Orifice 5
%mu = 2.3779*10^-5; %Orifice 7
nu = mu / rho_f; % Kinematic visc(v)
R = 461.526; % Universal gas constant [J/kmolK]
T = 723; % Fluid temp [Kelvin] @ inlet
%T = 679.78394; % @ Orifice 5
%T = 659.69409; % @ Orifice 7
P = 138;     % Inlet pressure
%P = 69;       % Pressure @ orifice 5
%P = 42;       % Pressure @ orifice 7
m_dot = 0.0355; %mass flow rate

d_h = 0.0025; %Hydraulic diamater inlet orifice
%d_h = 0.003;  % @ Orifice 5
```

```
%d_h = 0.004;  % @ Orifice 7
u = m_dot/(rho_f*((pi*d_h^2)/4)); %velocity


% Particle diameters [m]
%d_p = 1e-9;
%d_p = 1e-8;
d_p = 1e-7;


% Development of flow and particle parameters
Re_f = (rho_f * u * d_h)/(mu); % Reynolds number
Int = 0.16*(Re_f)^(-1/8);         % Turbulence intensity
l = mu * ((pi*M)/(2*R*T))^0.5; % Mean free path
Kn = l ./ d_p;                  % Knudsen number
Cc = 1 + Kn.*(2.514 + 0.8 .* exp(-0.55./Kn)); % Cunningham slip correction factor

k = 1.38054 * 10^-23; % Boltzmann constant
D_b = (k*T*Cc)/(3*pi*mu*d_p); % Stokes-Einstein equation diffusion coeff.

tau_p = (rho_p * d_p^2) / (18*mu); % Particle inertia relaxation time
tau_p2 = tau_p * Cc; % Accounting for rarefied gas effects

stk = (u*tau_p2)/d_h;     %Stokes number
sc = nu/D_b;            % Schmidt number

% Silica concentration calculated by the correlation of Fournier

A = -4.66206 +(0.0034063*T)+(2179.7*T^(-1))-(1.1292*10^(6)*T^(-2))+(1.3543*10^(8)*T^(3));
B = (-0.0014180*T) - (806.97*T^(-1));
C = 3.9465*10^(-4)*T;
v = (R*T)/(P*M);        %specific volume of the solvent

m = A + B*(log(v)) + C*(log(v))^2;     %molal silica concentration
sil_conc = log(m);      % silica concentration in mg/kg

m_p = sil_conc*10^-6*m_dot;     %mass flow rate of particle in kg/s
```

Appendix C

Evaluation of the master thesis

This master thesis is an thesis consisting of understanding and designing a numerical model using CFD. As aforementioned in the introduction 1, the background of CFD of the author was non-existing before starting on this master thesis. As a result, the first weeks of the semester went to attempt to understand the basic fundamentals of CFD, before moving on to an introductory Ansys Course arranged by the University of Yale. After some weeks, knowledge creating simple geometries and the simulation of the respective fluid flow had been obtained. However, the geometry in this present study is not a simple 2D pipe, making the whole process even more complex. Instead of basic axisymmetric flows, special considerations regarding the flow had to be accounted for. Both reversed and undeveloped flow were encountered, and solutions to counteract these problems had to found.

It should also be noted that the importance of a good mesh, should have been emphasized and understood earlier in master thesis process. Subsequently, the poorer mesh led to several errors during the simulations. After reading on several forums, watching innumerable amount videos on the internet and discussions with the supervisors, a better understanding of the usage of the different meshing methods and the mesh quality factors had been obtained. This also led to a satisfactory good representation of the fluid flow for the cascade impactor. However, when an adequate mesh had been obtained the number of cells had risen to approximately 2.5 million, and the computational time using a personal computer went over 24 hours. This took a long time, and it was not until after several simulations that it was decided that it would be both smart and time saving to borrow a computer at the facilities at NTNU. I.e., by borrowing this computer sooner, would have resulted in a more time efficient work.

The implementation of particles into the fluid flow using the Lagrangian method was also unknown to the author. Extensively time went by to learn and implement this into the Fluent application, together with obtaining an understanding of how particle deposition could be investigated.

Essentially, this master thesis consisted of two parts. Firstly, the learing and understanding of the fundamentals of CFD and Ansys. Secondly, the development of the numerical model in the present study. Overall, this master thesis have been both challenging and demanding, with a sudden and steep learning curve, but at the same time it has been quite interesting and a lot of new knowledge have been obtained.

NTNU

Norwegian University of
Science and Technology